DYNAMIC INVESTIGATION OF CU50AT%AU (001) ALLOY NANO-OXIDATION BY *IN SITU* UHV TEM

by

Liang Wang

B.S., Tsinghua University, 2000

Submitted to the Graduate Faculty of

School of Engineering in partial fulfillment

of the requirements for the degree of

Master of Science

University of Pittsburgh

2005

UNIVERSITY OF PITTSBURGH

SCHOOL OF ENGINEERING

This thesis was presented

by

Liang Wang

It was defended on

March 21, 2005

and approved by

Dr. John A. Barnard, Professor, Department of Materials Science and Engineering

Dr. Jörg M.K. Wiezorek, Associate Professor, Department of Materials Science and Engineering

Thesis Advisor: Dr. Judith C. Yang, Associate Professor, Department of Materials Science and Engineering

DYNAMIC INVESTIGATION OF CU50AT%AU (001) ALLOY FILM NANO-OXIDATION BY *IN SITU* UHV TEM

Liang Wang, M.S.

University of Pittsburgh, 2005

Elucidating the oxidation mechanism of alloy has significant practical and theoretical impact. The addition of alloying elements could substantially alter the oxidation behavior of the base metal. The aims of this thesis research are to model alloy oxidation by investigating Cu-Au oxidation using an *in situ* ultra-high vacuum transmission electron microscopy (UHV-TEM). Cu-Au system was chosen because 1) Au does not form stable oxide at the reaction conditions, thus only Cu is expected to oxidize; and 2) Our extensive prior experiments of Cu nano-oxidation.

The main findings of the research on $Cu_{0.5}Au_{0.5}$ (001) oxidation as compared to Cu (001) are: 1) segregation of gold atoms to the surface delays adsorption of oxygen and thus delays the nucleation (longer incubation time); 2) addition of gold enhances the nucleation by reducing nucleation activation energy (fast nucleation rate); 3) Oxide island growth is initially limited by surface oxygen diffusion. As oxide grows, a gold build-up zone forms around the oxide and hinders further growth by inhibits Cu supply to the reaction front; 4) Oxide grows slower due to the presence of gold.

TABLE OF CONTENTS

LIST OF TABLES

LIST OF FIGURES

PREFACE

My first, and most earnest, acknowledgment must go to my advisor, Prof. Judith C. Yang for her supervision, and financial support. For the past two and half years Prof. Yang has been really supportive and considerate.

My special thanks go to the Frederick Seitz Materials Research Laboratory, the University of Illinois at Urbana-Champaign, where all the experimental work in this thesis was carried out. I would like to thank I. Petrov, R. Twesten, K. Colravy, S. MacLaren, M. Marshall, M. Williams, J.G. Wen, B.Q. Li, and T. Banks for their generous technical assistance and discussion. Also I own my appreciation to all my friends in UIUC, H. Chen, Z.B. Ge, J.W. Liu, K. Zhao, W. Zhang, J. Tao, G.Z. Zhang, and P.G. Wu for their countless help.

I would like to thank Dr. G.W. Zhou for training me on the environmental TEM. Also I would like to thank him and Dr. J.A. Eastman from Argonne National Laboratory for synthesizing $Cu_{0.62}Au_{0.38}$ thin films.

The time spent by the committee members and their suggestions to improve the thesis are all very much appreciated.

I am grateful to my colleagues and friends in the University of Pittsburgh, L. Li, F.T. Xu (and his wife P.P. Ye), J.H. Wu, X.T. Han, L. Sun (and her husband C. Fang), W. Gao, M. Kisa, and R. McAfee, for their assistance on countless occasions.

Finally, and most heartfelt, acknowledgment must go to my family. They are always there whenever I need them. This could not be done without them. They have my everlasting love.

1.0 INTRODUCTION

1.1 GENERAL INTRODUCTION

Classic investigations of the oxidation behavior of metals are mostly based on thermogravimetric analysis (TGA), which measures weight changes but not structural changes. Hence, classic models of oxidation assume uniform oxide film growth, yet it is well known that many metals form oxide islands (e.g. Ni [1, 2], Fe [3-5], Pd [6] and Ti [7]) initially that later coalesce into an oxide scale. The nucleation and growth processes of oxides (which is referred as nano-oxidation hereafter) are particularly important because they impact many diverse materials problems, from passivation properties [8, 9], gate oxides [10], and fuel cell reactions to the synthesis of self-assembled nano-oxide structure for optical [3], magnetic [4] or catalytic performance [11, 12].

Many elegant surface science studies have been performed using UHV scanning tunneling microscopy (STM) to watch the interaction of gases, including oxygen, on bare metal surfaces. [6, 13-15], but these studies only extend to a few monolayers.

Nevertheless, it has been recognized for a long time that the mechanism of initial stage oxidation, i.e. from the nucleation to the coalescence of thermodynamically stable oxides that occurs in the nanometer scale regime, plays a vital role in the oxidation behavior at later stages of various metals. [6, 11] Elucidating the oxidation mechanism in this transient stage would bridge the information gap between surface science study and traditional thermogravimetric analysis, and

thus provide understanding of metal oxidation from nucleation on the surface to the growth of the oxide scale.

By using *in situ* UHV-TEM with clean, well controlled reaction conditions and nanometer resolution, information inaccessible to both surface science study and traditional oxidation methods, can be ascertained. Previous works by Yang *et al.* [16-19] and Zhou *et al.* [7, 17, 19], using Cu as a model system, clearly demonstrated that heteroepitaxial concepts, used for film growth, also describes surprisingly well the nano-oxidation of metals where oxygen surface diffusion is the dominant mechanism of initial transport, nucleation and growth. By primarily using *in situ* UHV-TEM, Yang [16-19] and Zhou [7, 17, 19] have revealed a vast range of information regarding kinetics of oxide formation, their size and shape evolution, temperature, pressure and crystal orientation effects, as well as the environmental stability of the oxide.

However, many engineered materials are alloys; hence, it is critical to understand how the nucleation and growth processes of the oxides during oxidation of an alloy are affected by the presence of secondary elements, such as preferred nucleation sites in multiphase system, composition of the nucleus of a system with more than one active alloying elements, and the redistribution of alloy elements during oxide growth.

In this thesis, *in situ* studies of the initial oxidation behavior of copper-based alloys were carried out. Cu50at%Au ($Cu_{0.5}Au_{0.5}$ hereafter) (001) single crystal thin films were oxidized to model alloy nano-oxidation because of the in-depth understanding of Cu oxidation dynamics and also because both clean and oxygen modified surface structures of Cu-Au alloys have been extensively investigated [20-26]. Since Au is stable and miscible to Cu within the composition and temperature range which we investigated, only Cu_2O is expected to form uniformly in the Cu-Au alloy, which is similar to Cu oxidation. However, many differences exist between Cu and

Cu-Au that are pivotal to surface processes and, hence, will impact nano-oxidation dramatically. These differences include: 1) lattice constant (thus lattice mismatch and interfacial strain energy); 2) surface energy; 3) segregation of Au to the surface (driven by the lower surface energy of Au; 4) diffusion of Au and Cu during oxidation that will affect oxidation kinetics; 5) limited supply of Cu that may lead to self-limited growth of oxide; and 6) effect of Au on Cu activity.

1.2 OXYGEN SURFACE DIFFUSION MODEL OF NANO-OXIDATION

Yang *et al.* [16-19] proposed and demonstrated that heteroepitaxial concepts used to describe thin film growth, e.g. Ge on Si, can successfully describe the initial oxidation of Cu (001) where oxygen surface diffusion is the primary transport mechanism. Both nucleation of Cu_2O and oxide growth are controlled by oxygen surface diffusion.

1.2.1 Heteroepitaxy of Cu_2O on Cu and $Cu_{1-x}Au_x$ surfaces

There are three possible heteroepitaxial growth modes, depending on the surface energy and lattice mismatch between the epilayer and the substrate, i.e. monolayer-by-monolayer growth mode (Frank-van der Merve or FM mode), 3D island growth (identified as Volmer-Weber or VW mode), and an intermediate case which was found by Stranski and Krastanov (SK mode) where 2D growth initially occurs followed by 3D island formation. The most important factor in determining growth mode is the strain. Ge/Si is one of the most extensively investigated SK heteroepitaxy system because it is one of the most promising system for self-assemble of Ge "quantum dots" for electronic and optoelectronic applications [27]. Figure 1.1 (a) shows Ge islands growing on Si (001) surface at 302 ºC investigated by STM [27]. Figure 1.1 (b) is the

nano-oxidation of $Cu_{0.5}Au_{0.5}$ (001) at 550 ºC with oxygen partial pressure of 5×10^{-4} torr by *in situ* TEM. In fact for all temperatures, low index Cu surfaces [7, 19, 28, 29] and compositions of $Cu_{1-x}Au_x$ (x ranges from 0 to 0.5) alloys films investigated, Cu_2O islands form on Cu and $Cu_{1-x}Au_x$ with cube-on-cube crystallographical orientation relationship. When compared with Ge/Si, they have striking similarities. First of all, in both cases islands grow epitaxially on the substrate (e.g. diffraction pattern in Figure 1.1 (b)). Secondly, the nucleation and growth of the islands are diffusion limited. Hence the same heteroepitaxial concept could also be used for describing nano-oxidation of Cu or Cu-Au alloy.

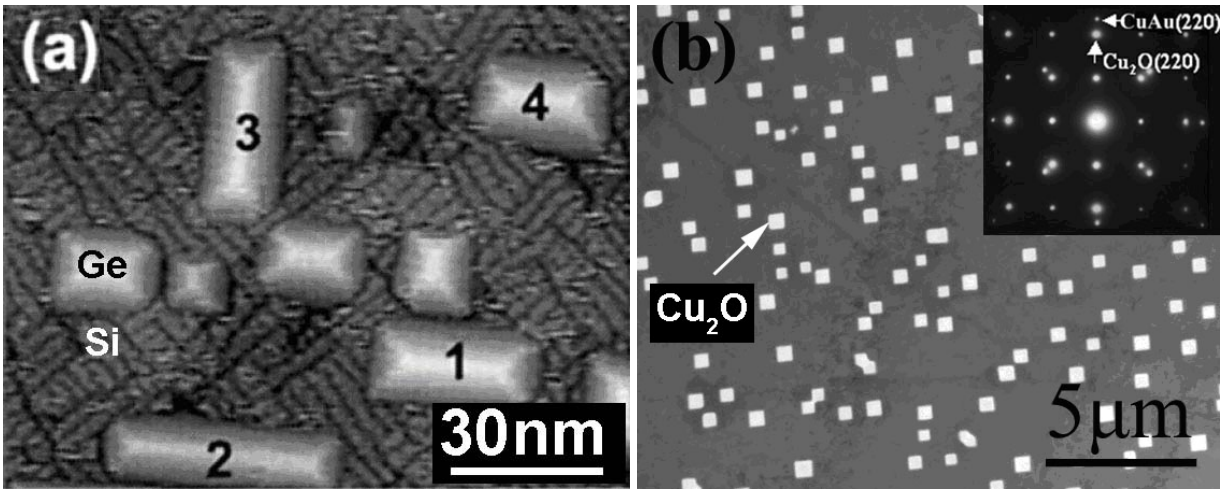

Figure 1.1 Heteroepitaxial growth of (a) Ge islands on Si (001) surface. [27] (b) Cu_2O islands grow on $Cu_{0.5}Au_{0.5}$ (001) surface at 550 ºC

1.2.2 Oxide Nucleation

After admitting oxygen gas into the TEM column, the nuclei appear after an incubation time (τ_0) ranging from tens of seconds to several minutes. During this incubation time, O_2 molecules striking the film will dissociate, diffuse on the surface, and may be lost to re-evaporation, form a new nucleus, or be incorporated into an existing Cu_2O island. Regardless of the details of the intermediate steps, the density of these stable nuclei is expected to increase with time, reach a saturation density, N_s, and then decrease as the discrete nuclei grow into larger islands and coalesce. Therefore, one consequence of oxygen surface diffusion controlled nucleation is that there is a saturation island density, $1/L_d^2$, where L_d^2 is the area of the "oxygen capture zone" or "denuded zone" around each Cu_2O island. An oxygen concentration gradient exists across this zone such that oxygen that lands within this zone would diffuse to the Cu_2O islands and no other nucleation event is permitted inside this denuded zone; hence, the oxide islands act as oxygen sinks.

By assuming oxygen surface diffusion is the dominant mass transport mechanism for oxide nucleation, Yang, *et al*. demonstrated that the probability of an oxide nucleation event is proportional to the fraction of the available surface area outside these "zones of oxygen capture" and the oxide nucleus density can be determined to be [30]

$$N = \frac{1}{L_d^2}\left(1 - e^{-kL_d^2 t}\right) \qquad \text{Equation 1.1}$$

where L_d^2 is the area of the zone of oxygen capture, $1/L_d^2$ is the saturation island density, L_d is much larger than the diameter of the oxide island, k is the initial nucleation rate, which depends on the probability for Cu and O to form Cu_2O at the oxidation temperature, and t is the reaction time.

The saturation island density depends on temperature and follows an Arrhenius relationship [31],

$$N_S \propto \exp(-\Delta G^* / kT) \qquad \text{Equation 1.2}$$

where k is Boltzmann's constant, and T is the oxidation temperature. ΔG^* is the Gibbs free energy change to form a critical nucleus (or activation energy of nucleation) in classic nucleation theory. ΔG^* of the nucleation depends on the energies of nucleation, surface/interface energies and elastic energy changes. By Venables' nucleation rate theory [32], this ΔG^* can incorporate surface diffusion energy, nucleation energy, and desorption energy. By plotting the saturation island density at different temperatures, ΔG^* for this diffusion limited nucleation process can be determined. Also, this activation energy can also be obtained by computer simulation such as Kinetic Monte Carlo [33].

1.2.3 Oxide Growth

Orr, [34] followed by Holloway and Hudson [35], has developed an oxidation model based on the assumption that oxygen surface diffusion should play a major role in the initial growth of the metal oxide. They assumed that the 2D oxide islands grew on the metal surface and obtained a parabolic growth rate law if oxygen surface diffusion is the dominant mass transport mechanism and the reaction only occurs at the islands perimeters.

Orr's model can also be extended to 3D islands growth. Following the derivation of Orr, oxygen surface diffusion to the perimeter of an oxide island generates a growth rate [34],

$$\frac{dN(t)}{dt} = 2\pi r C_S f_S, \qquad \text{Equation 1.3}$$

where $N(t)$ is the number of oxygen atoms in a Cu_2O island at time t, r is the radius of the circular profile of an island, C_s is the sticking coefficient of oxygen to a Cu_2O island, and f_s is the

diffusive flux of oxygen. For 2-D lateral growth of a disk-shaped island, with thickness *a*, then by solving the above differential equation, we see that the cross-sectional area increases parabolically with respect to time [34]. Following a similar analysis for 3-D growth of a spherical island, then the cross-sectional area, *A*, of the oxide island, is

$$A(t) = \frac{\pi\Omega C_S^2 D C_0}{D + L_d C_S}(t - t_0), \qquad \text{Equation 1.4}$$

where Ω is the volume occupied by one O atom in Cu_2O, C_o is the surface concentration of oxygen far away from the Cu_2O islands, *D* is the surface diffusion coefficient of oxygen, L_d is the radius of the zone of oxygen capture. The power law dependence, t^2 for 2D and *t* for 3D, is independent of the shape of the island. On the other hand, if we know the scaling law dependence of projected areas of islands with time, it would be easy to determine whether the growth is 2D or 3D especially for TEM observation where no 3D information can be achieved.

1.3 *In Situ* STUDY OF Cu NANO-OXIDATION

1.3.1 Temperature Effect on Oxide Morphology

The temperature effect of Cu_2O islands morphologies by oxidizing Cu (100) films have been systematically studied by Yang [18], Zhou [19] and Sun [36] on the same *in situ* UHV TEM. Figure 1.2 is a reprint of the bright field (BF) TEM images from Ref. [19], which shows the morphology of Cu_2O islands formed on Cu (001) surface at different oxidation temperatures. Actually, from 200 to 350 ºC [18, 19, 36], only triangular islands formed (Figure 1.2 (a)). The long edge of the triangle is indexed to be along [110] direction and the short edges are [100] and [010]. The island size increased with continued exposure to oxygen, but the island shape did not

change. At elevated temperatures, between 400 and 550 ºC, the islands exhibited a shape change from triangular to square- or round-based islands (Figure 1.2 (b)). In a narrow temperature regime near 600 ºC, elongated 1D Cu_2O rods formed as shown in Figure 1.2 (c). The shape formation mechanism can be explained by the energy model proposed by Tersoff and Tromp [37] where the elongated islands can efficiently release elastic strain energy stored in the oxide. Oxidation at temperatures between 650 and 800 ºC resulted in the formation of dome islands, which have a distinctive cross-hatched pattern as shown in Figure 1.2 (d). At around 1000 ºC, hollow terraced pyramid structure was observed, where the terrace has roughly equal step width. It is proposed that the terraced structure is formed by periodic release of compressive strain energy by slip along certain lattice plane at high temperature.

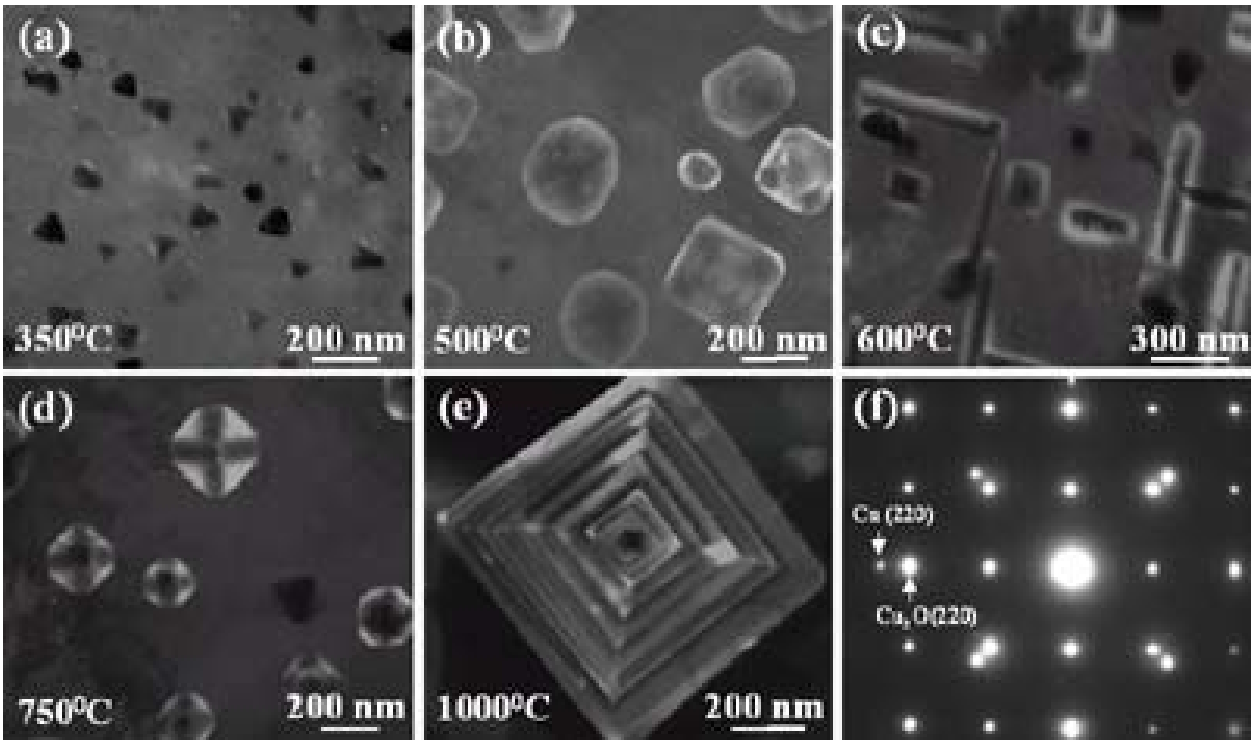

Figure 1.2 The morphology of Cu_2O islands formed during *in situ* oxidation of Cu(001) at an oxygen partial pressure of $5x10^{-4}$ torr and oxidation temperatures of (a) 350°C, (b) 500°C, (c) 600°C, (d) 750°C and (e) 1000°C, (f) epitaxial relationship between Cu_2O and Cu(100). Reprint from Ref. [19].

Proposed by Zhou *et al.* [19] that, energetically, balance between surface/interface energy and elastic strain energy determines the final shape of the islands. Cu_2O has a thermal expansion coefficient of 1.9×10^{-6} K^{-1}, and Cu 17×10^{-6} K^{-1} [38]. With increasing temperature, the lattice mismatch becomes smaller, and the lattice mismatch induced strain becomes smaller correspondingly. This could explain the triangular shape at low temperatures, where the strain is high and so the interface area is minimized by this triangular shape. At higher temperatures, there is less lattice mismatch and therefore reducing interfacial strain with increasing

temperatures. Hence, the chosen interfaces will be along the low energy interfaces (such as the low index planes). Another effect of temperature is on the mechanical properties of the oxide and substrate. At higher temperatures, the metal substrate and oxide become significantly more ductile. The enhanced ductility at higher temperatures provides a mechanical mechanism for strain relaxation that should affect the oxide morphology development. [19]

1.3.2 Surface Orientation Effect

The initial oxidation of metal/alloy is a surface process where oxygen diffusion, oxide nucleation, and growth all occur on the alloy surface, thus the atom arrangement on the surface, i.e. surface orientation and surface composition have significant impact on the oxidation kinetics and energetics.

Gwathmey and co-workers [39-41] have demonstrated that the oxidation phenomena observed on copper vary with crystal orientation. Investigations by Benard and co-workers [42, 43] showed that the rates of oxidation were different for different crystal orientations. Zhou *et al.* [7, 28, 29] did a systematic investigation of the kinetics of the initial oxidation on Cu (100), (110) and (111) surfaces. The dependence of island density on oxidation time, saturation island density on oxidation temperature, and island growth as a function of oxidation time were all studied.

Many investigations have elegantly demonstrated that metal surfaces experience a reconstruction due to the oxygen chemisorption. Oxygen chemisorption on Cu(100) and Cu(110) results in restructuring of a surface with $\left(\sqrt{2}\times 2\sqrt{2}\right)$R45º O-Cu(100) and (2×1) O-Cu(110) surface structures [44-48]. The $\left(\sqrt{2}\times 2\sqrt{2}\right)$R45º O-Cu(100) has a more compact oxygen chemisorption than (2×1)O-Cu(110) surface which has a corrugated structure. Therefore, the activation barrier for surface diffusion of oxygen could be higher on the Cu(110) surface than the Cu(100). The

smaller oxygen surface diffusion coefficient results in a smaller capture zone of oxygen and creates a higher nuclei density on Cu(110) than Cu(100). Furthermore, the "corrugated" Cu(110) surface could provide more preferential nucleation sites than Cu(100), and thereby lead to greater island density.

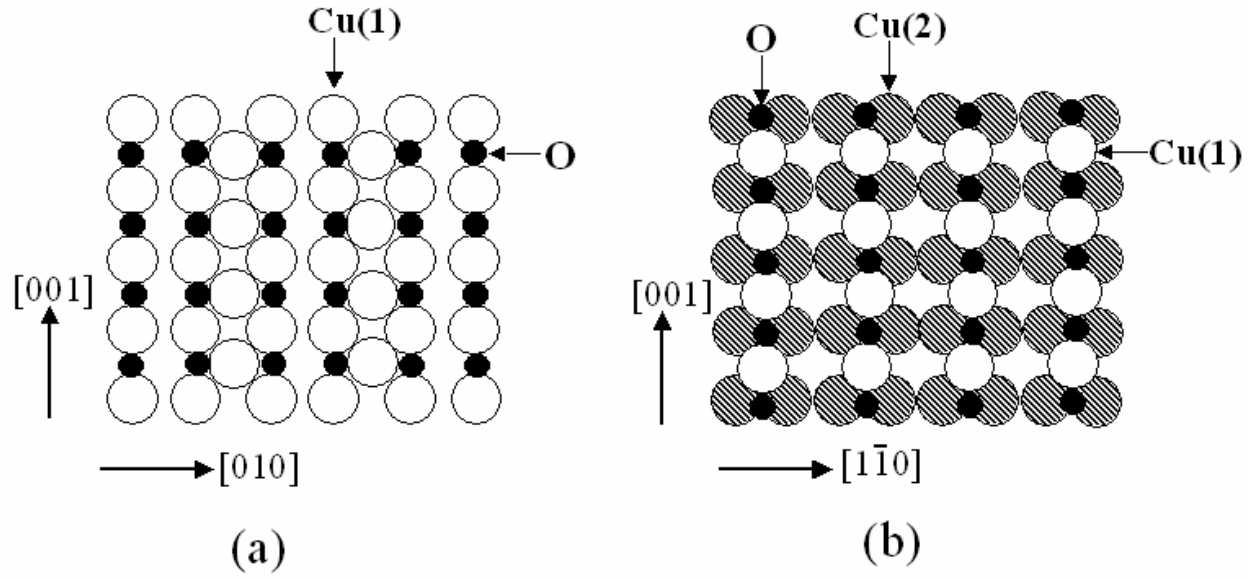

Figure 1.3 Schematic diagram of the reconstructed $\left(\sqrt{2}\times 2\sqrt{2}\right)$R45º O-Cu(100) surface (a), and (2×1)O-Cu(110) surface (b) due to oxygen chemisorption. Filled circles: O atoms; open circles: top layer Cu atoms; shaded circles: second layer Cu atoms.

Cu (110) surface undergoes a roughening process at ~710 ºC which is typically characterized in terms of the appearance of hills and valleys of arbitrary height on the surface by the thermal generation of atomic steps at the roughening temperature. Oxide formed at both below and above this transition temperature shows trapezoid projected shape (Figures 1.4a,b). Kinetics studies show that the surface oxygen diffusion describes the oxidation on these surfaces equally well.

When the temperature is raised to ~800 ºC a more aggressive surface morphology change, namely faceting, occurs. During faceting a flat surface breaks into facets of different orientations due to thermodynamic instability at elevated temperatures or adsorption of chemical species, and it is generally believed that driving force for the faceting is the anisotropy of the surface free energy [49, 50]. Experiments show that oxide nucleation occurs preferentially at the valleys on the surface [51] where the nucleation activation energy is minimized. The oxide grows also preferentially along the grove.

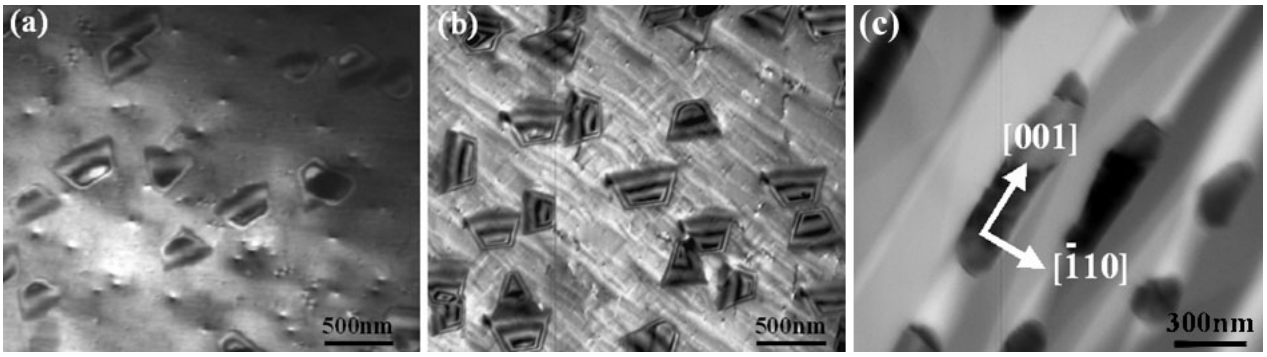

Figure 1.4 TEM micrographs of oxide islands formed on (a) flat Cu(110) surface (650 °C); (b) thermally roughened surface (750 °C); and (c) faceted surface (800 °C) at the same oxygen pressure (5×10^{-4} torr) and oxidation time (~10 min) [7].

Cu (111) surface has a more complicated structure. Between 200-350ºC the chemisorption of oxygen on Cu(111) results in '29'-$\left(\sqrt{13}R46.1^\circ \times 7R21.8^\circ\right)$ and '44'-$\left(\sqrt{73}R5.8^\circ \times \sqrt{21}R-10.9^\circ\right)$ lattice structures [52-55]. These structures comprise distorted hexagonal arrays of O atoms arranged in parallel lines in the first layer, with the unit cell areas 29 and 44 times larger than those of the substrate Cu(111), which appears strikingly similar to the (111)Cu_2O structure. Both

chemisorbed oxygen layers were considered to be analogous to the planes of the $Cu_2O(111)$ which has a structure with equilateral hexagons of oxygen atoms in the first layer. Therefore, the reconstructed Cu{111} surface is almost a template for the Cu_2O {111} structure, which facilitates the nucleation of the Cu_2O structure and gives rise to a fast initial nucleation rate of oxide islands.

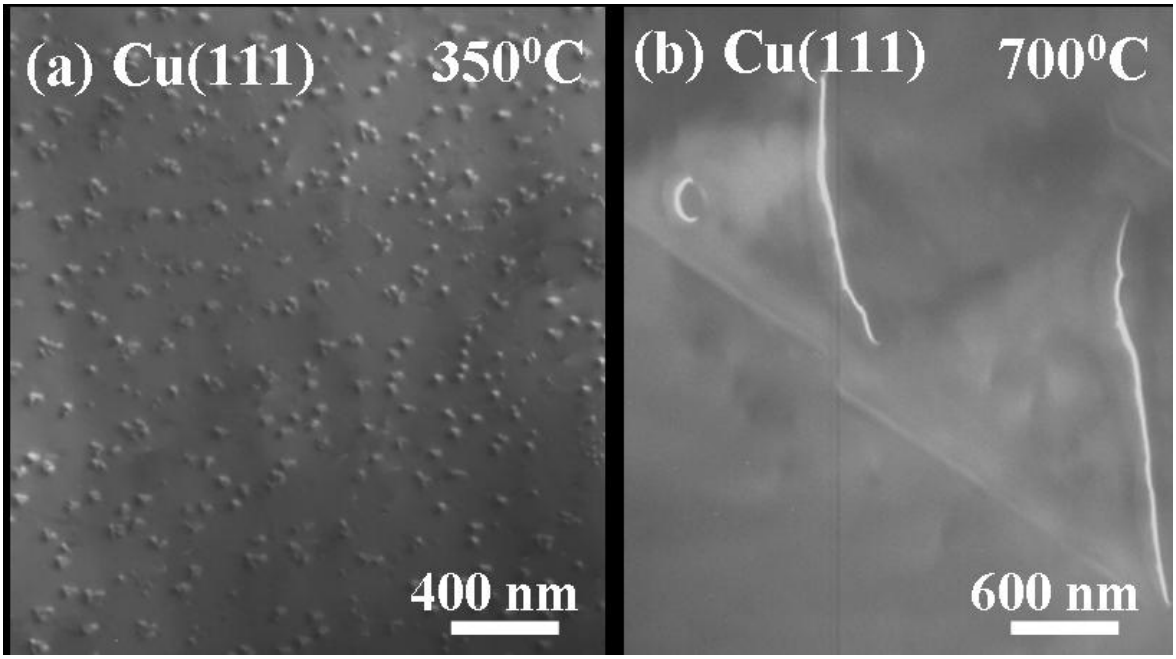

Figure 1.5 TEM micrographs of oxide islands formed on Cu (111) surface at different temperature. (a) at 350 °C island growth with high saturation density; (b) at layer growth.800 °C [7].

1.4 SURFACE STRUCTURE OF $Cu_{1-x}Au_x$ BEFORE AND AFTER O_2 EXPOSURE

Cu-Au alloy is one of the most widely studied alloy system with compositional order-disorder phase transition at T_C (T_C=410 ºC for Cu50at%Au bulk alloy). As shown in the phase diagram of Au-Cu binary system (Figure 1.6), both bulk $Cu_{0.25}Au_{0.75}$ and $Cu_{0.75}Au_{0.25}$ assume ordered $L1_2$ structure (shown in Figure 1.7 (b)) when $T<T_C$, while $Cu_{0.5}Au_{0.5}$ assumes $L1_0$ structure (Figure 1.7 (a)) below 410 ºC. Above the order-disorder transition temperature Cu and Au are miscible and the bulk alloy has face-centered cubic (FCC) structure. The temperature range of current thesis work is denoted in Figure 1.6 by the double arrow.

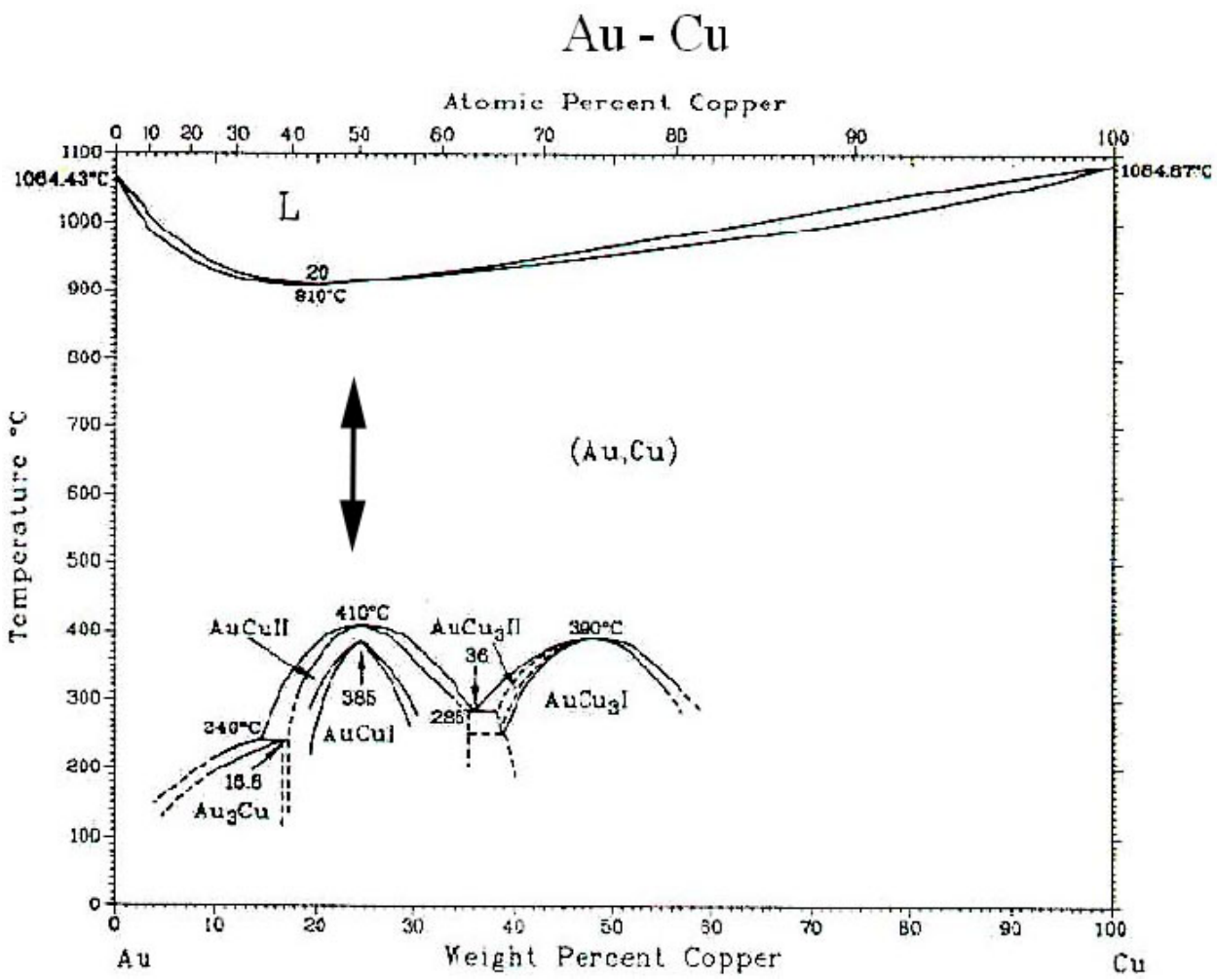

Figure 1.6 Au-Cu phase diagram. The arrow denotes the composition and temperature range of present work. Also note that the order-disorder transition temperature for bulk Cu50at%Au is 410 ºC.

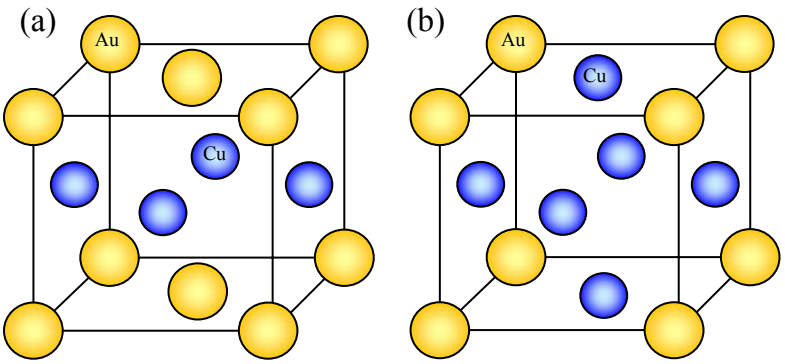

Figure 1.7 Atom arrangement in (a) $Cu_{0.5}Au_{0.5}$ $L1_0$ and (b) $Cu_{0.75}Au_{0.25}$ $L1_2$ structure.

Cu-Au alloy surface has been extensively studied both experimentally and theoretically. For clean (001) $Cu_{1-x}Au_x$ thin film, Au atoms segregate to the topmost layer because of its lower surface energy (See Ref. [20-22]), while Cu enriches the second layer to maximize short-range ordering [23], then Au-rich again, and so forth (see Figure 1.8). This configuration results in a layer-by-layer structure consisting of alternating (001) layers of Au-rich and Cu-rich composition. The depth of this oscillatory concentration profile is highly temperature dependent [20]. As expected, below T_C, the oscillatory concentration profile extends throughout the film in $Cu_{0.5}Au_{0.5}$. Above T_C, the depth decreases as temperature increases since the entropy contribution to free energy favors a random arrangement. Nevertheless, Au still has a higher concentration in the topmost layer than the bulk even above T_C. From previous surface science studies [20-23] the topmost layer of the surface is rich in inert Au than the bulk. Our thin film sample has two surfaces. This configuration has no impact on the oscillatory concentration profile, since above T_C the oscillatory profile extends only <10 layers (~2 nm) into the bulk of the film which is significantly smaller than the thickness of the film presently used. [20]

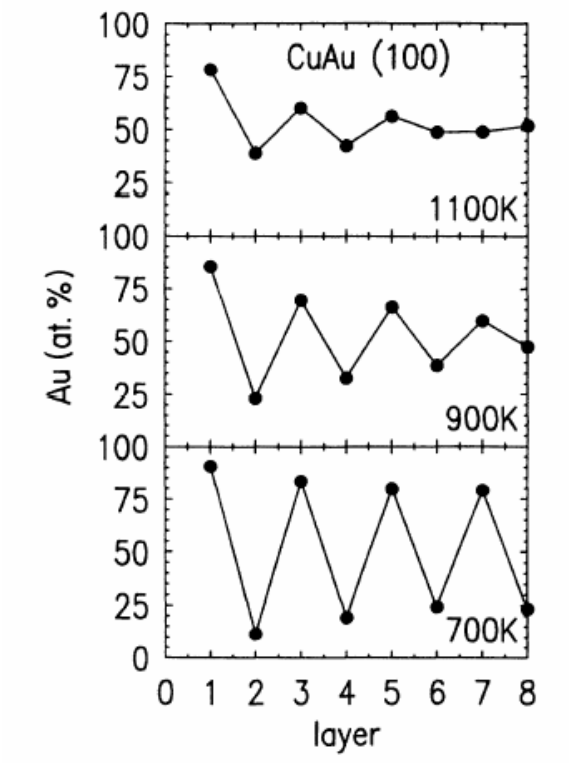

Figure 1.8 Calculated alloy composition for each layer at the CuAu (001) surface [20]. Note that the temperature in current work falls between 900 K and 1100 K.

The segregation of Au should significantly alters the oxidation kinetics of Cu-Au alloy since Au rich surface is inert for oxygen adsorption and dissociation especially at low temperature when Au concentration on the surface is higher [24].

2.0 PROJECT OBJECTIVES

To bridge the gap between information provided by surface science study and that provided by traditional thermogravimetric analysis, the initial stages of metal oxidation -- from nucleation to coalescence -- are investigated by *in situ* UHV-TEM. *In situ* UHV-TEM is capable of obtaining real-time information on structure evolution with nanometer resolution, while UHV environment provides clean and well controlled reaction conditions. Both are irreplaceable for investigations of nano-oxidation.

The objective of this study is to investigate the nano-oxidation kinetics and energetics of $Cu_{1-x}Au_x$ (001) single crystal alloy thin films. Although Au is miscible to Cu and Au is non-oxidizing in the composition and temperature range we investigated, significant differences exist when compared with pure Cu oxidation. By comparing with Cu oxidation kinetics, the effect of inert Au to oxidation of Cu in the initial stage can be deduced. Furthermore, although the present system involved is Cu-Au alloys, it is believed that these results have an interesting extension to the alloy systems containing one reactive component such as Fe, Ni, etc., and one noble component such as Pt, Ag, etc., which do not form stable oxides under normal conditions.

3.0 EXPERIMENTAL PROCEDURES

3.1 Cu-Au FILM PREPARATION AND SAMPLE MOUNTING

90-100 nm thick $Cu_{0.5}Au_{0.5}$ (001) single crystal films were synthesized by co-sputtering Cu (99.999%) and Au (99.99%) in an AJA sputtering system onto irradiated NaCl (001) substrate at the Materials Research Lab in the University of Illinois Urbana-Champaign. Cu and $Cu_{1-x}Au_x$ can be grown epitaxially, i.e. $(001)_{metal}//(001)_{NaCl}$, $<001>_{metal}//<001>_{NaCl}$, on rock salt if appropriate deposition rates and growth temperature are used [56-58]. Prior to deposition, the NaCl substrate was cleaved in air with a sharp knife along (001) plane. The deposition chamber has a base pressure of 10^{-8} torr. During deposition, the substrate temperature was maintained at 270-300 ºC with a total deposition rate of ~ 5 Å/s monitored by a quartz crystal microbalancers (QCM) while the Ar gas pressure was maintained at 5 mtorr. After deposition the film was annealed at the same temperature for half an hour. The thickness and composition were calibrated by Rutherford Backscattering Spectrometry (RBS) which has an accuracy of 2-4%. The films were cleaved into the desired size and then floated off the rock salt in deionized water. Residual rock salt on the films was removed by transferring the films into fresh water several times. They were then floated onto the sample supports, depicted in Figure 3.1 (a), which are lithographically produced Si pieces, 350 μm thick and 2 by 3 mm in size, with a 1 μm Si_3N_4 layer on top. The size of the central hole extended from 400 μm by 400 μm on top to 800 μm by

800 μm at the bottom of the Si piece. Once the water had dried off, the sample could be mounted onto the sample cartridge (Figure 3.1 (b)).

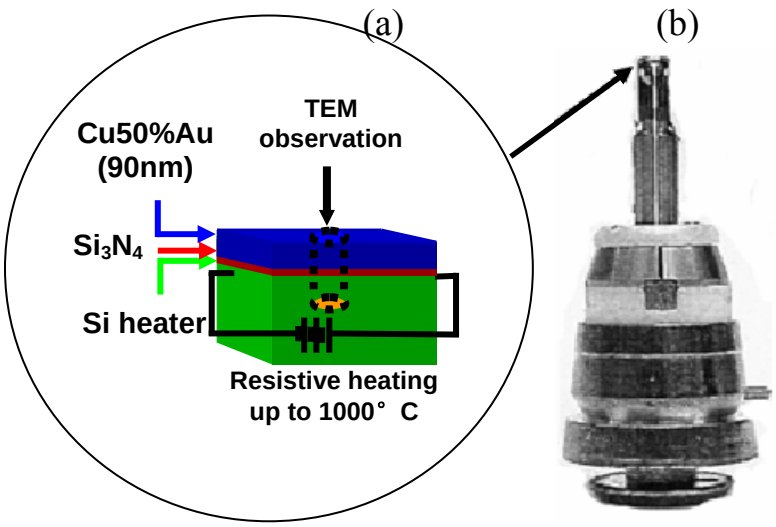

Figure 3.1 (a) Si sample support and (b) sample cartridge. In the microscope, the sample cartridge was mounted upside down.

Two metal posts, electrically isolated, supported the sample, which was secured in place by two spring-loaded clips. Once the sample cartridge was inserted into the polepeice, springs pressing against the lower part of the cartridge ensured electrical contact. A layer of Si_3N_4 on Si surface ensures no current passing through the metal film. The sample was heated by passing a current through the Si support. Therefore, care had to be taken that the metal film did not cause a short circuit. The design of the microscope, especially the top entry mechanism, did not allow for a thermocouple attachment to measure the sample temperature. Therefore, it was necessary to rely on a calibration curve which related the power ($P=I\cdot V$) across the sample to the actual temperature. This type of temperature measurement, however, depends strongly on the geometry

and material of the sample support. The varying sizes of the metal thin films on top of the Si_3N_4 should not affect the temperature measurement significantly. In order to perform the temperature calibration, a sample was mounted in the cartridge, which was then placed inside a bell jar evaporator. A thermocouple was attached to the sample and electrical connections were made to the cartridge to measure T as a function of the power passed through the Si holder. Furthermore, temperatures above 800 K were also measured with an infrared pyrometer through the glass jar, which were in good agreement with the thermocouple measurements. The voltage could not be measured directly across the sample and therefore included the voltage drops due to contact resistance to the sample itself. The resistance calculated from the measured current and voltage values, nevertheless, were consistent with the temperature-resistance dependence of a semiconductor [59]. This implies that any contact resistance is small and can be neglected. Additional temperature measurements were calibrated with the phase transition temperature of Cu_3Au [59].

3.2 *In Situ* UHV-TEM

The primary facility for studying the oxidation of the alloy films was an *in situ* UHV-TEM, as shown in Figure 3.2, and the main elements of the system are illustrated in the schematic drawing (Figure 3.2 (b)). The electron microscope is a modified JEOL 200CX TEM with a top entry sample holder [60]. The additional pumping on the sample chamber consisted of a combined Thermionics ion/liquid nitrogen cooled sublimation pump and a Balzers turbomolecular pump. Furthermore, a cryoshield surrounds the specimen cartridge which is cooled via conduction through a Cu wire to a cold finger held at liquid nitrogen or liquid helium

temperature. The pressure in the sample region was determined by an ion gauge attached above the polepiece.

Typical pressures in the sample chamber were ~10^{-7} torr with just the turbo pump operating. The pressure could be improved by an order of magnitude by the ion pump. The best base pressure at the actual sample location inside the objective lens polepiece could not be measured directly, but the Si (001) (2×1) surface reconstruction was found to be stable for ≈40 min at room temperature with the liquid He cryoshroud operating [59]. Hence, a pressure in the low 10^{-9} torr range at the sample position can be inferred. Various gas sources, e.g., water vapor, methanol, hydrogen and oxygen could be introduced into the sample chamber with a manually controlled leak valve. The partial gas pressure up to 10^{-4} torr could be achieved with the electron beam operating. By isolating the TEM gun chamber, 760 torr partial pressure is achievable. For this thesis work, oxidation was monitored at oxygen partial pressure of 5×10^{-4} torr.

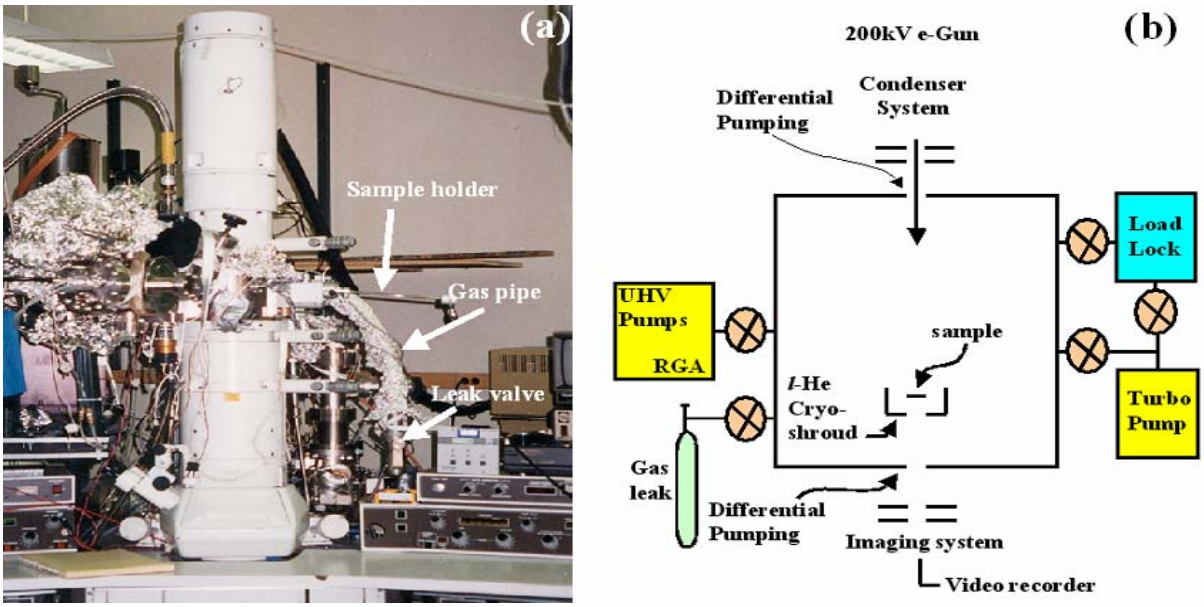

Figure 3.2 (a) The modified *in situ* UHV-TEM and (b) schematics of the main elements of the system.

During the experiments, the sample was first heated to the desired temperature and maintained for 10 minutes to ensure temperature stability. Then oxygen was admitted into the column at a partial pressure of 5×10^{-4} torr. TEM micrographs and diffraction patterns were recorded at regular intervals on to negatives which were then digitized with a Leafscan™ 45, and the software package NIH ImageJ™ was used to determine cross-section area of the oxide islands.

3.3 ATOMIC FORCE MICROCOPY

The surface topography of the films after oxidation was characterized by Digital Instrument Dimension 3100 Atomic Force Microcopy (AFM). Since the sample was free standing, special

care is need for AFM analysis. That is to minimize the force applied on the cantilever yet still get enough signal/noise ratio. In AFM, like in all scanning probe microscopy techniques, a sharp probe scans across the surface and the tip-sample interaction is monitored. AFM is usually done in one of two modes, contact mode or tapping mode. In current research all AFM analysis was carried out by tapping mode. The scan size is 512×512 pixels and the scan speed ranges from 1 Hz for 10×10 μm^2 scan to 2 Hz for 1×1 μm^2 or smaller scan size. The offline version of the software package Nanoscope III^{TM} was used for processing of the images.

3.4 NED AND STEM ANALYSIS

Ex situ Nanoarea Electron Diffraction (NED) and Scanning Transmission Electron Microscopy (STEM) analysis was carried out on JEOL 2010F TEM. The JEOL 2010F is an energy filtering, field-emission analytical TEM. The point-to-point resolution of the microscope is 0.24nm and the microscope is equipped with a STEM system and capable of tilting ±40 degrees on the x-axis and ±30 degrees on y-axis. It is ideal for small probe work including: STEM Z-contrast images (also called High Angle Angular Dark Field (HAADF)), NED, and spatially resolved Electron Energy Loss Spectroscopy (EELS) and Energy Dispersive X-ray Spectroscopy (EDS). It operates at 200kV and uses a Schottky field emitter. The 2010F is equipped with an energy filter to filter both images and diffraction patterns as well as act as an energy-loss spectrometer. The system is capable of EDS/EELS mapping, holography, and *in situ* heating and cooling. Both intensified video rate and slow-scan CCD cameras are available. The system is controlled by the JEOL FasTEM system allowing total computer control. Diffraction patterns is recorded on Fuji Imaging Plates (IP).

Figure 3.3 shows a schematic ray diagram for parallel beam NED [61]. A mini lens is inserted to focus the beam on to the front focal plane of the objective lens. The beam size is controlled by the size of the condenser aperture. A ~50 nm beam size can be achieved with 10 μm aperture, which is much smaller than conventional selected area electron diffraction (SAED), and does not suffer from aberration induced image shift [62].

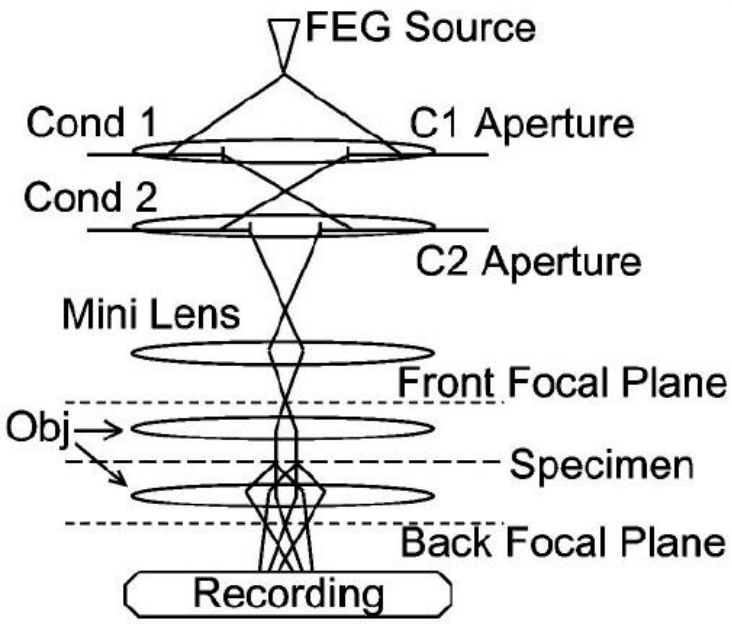

Figure 3.3 Schematic ray diagram of parallel beam NED. A mini lens is used to focus the beam on to the front focal plane of the objective lens. The beam size is determined by the size of the condenser aperture. [61]

Z-contrast images are formed by collecting high-angle elastically-scattered electrons with an annular dark-field detector (Figure 3.4). When operating in this mode, an electron beam with a size in nanometer scale rasters across the sample and an annular dark field detector collects the

incoherently elastically-scattered electrons. The scattered intensity is the sum of independent scatterings from individual atoms and is proportional to Z^2, so the incoherent images of the Z-contrast method are interpreted more directly in terms of atom types and positions.[63] It is a powerful tool to identify local chemistry in a multi-component system like the current work especially when combined with the structure characterization capability of TEM techniques.

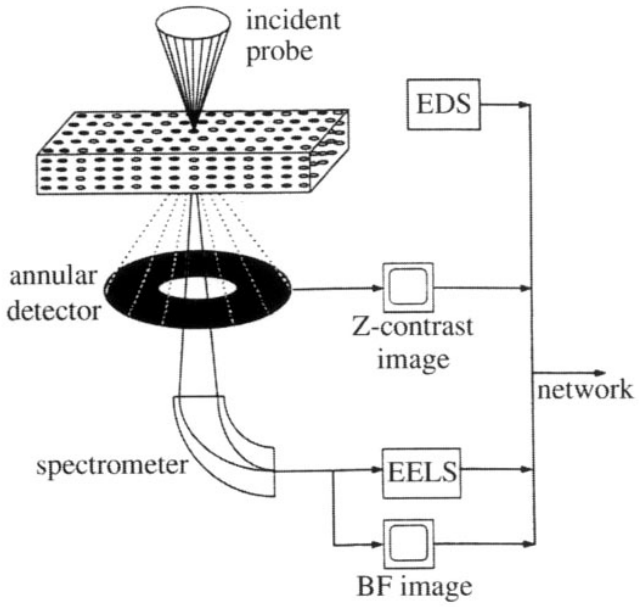

Figure 3.4 Schematic of an annular detector and EELS spectrometer in a STEM. [63].

4.0 RESULTS ON NANO-OXIDATION OF $Cu_{0.5}Au_{0.5}$ AND DISCUSSION

4.1 FILM STRUCTURE BEFORE OXIDATION

As depicted by bright field TEM image in Figure 4.1 (a), the film is single crystal and microscopically uniform. Below T_C (~410 °C), $Cu_{0.5}Au_{0.5}$ film assumes an ordered $L1_0$ tetragonal structure. Because in $L1_0$ structure $a = b \neq c$, there are two possible configurations--c axis normal to or c axis in the film plane--which can be distinguished by electron diffraction pattern. Figure 4.1 (b) is the diffraction pattern of the film at room temperature. Both four-fold symmetry and extinction of {100} type spots indicate that the c axis is normal to the film. Also, no diffraction spots from oxide are visible in the electron diffraction pattern indicating the film surface does not form a noticeable native oxide, as compared to Cu (001) [7]. Although no native oxide is found, the film is still annealed at 700 °C in the column with vacuum of 10^{-8} torr for 10 minutes prior to oxidation to make sure the film is clean. Upon heating to ~410 °C the {110} type superlattice spots gradually disappear demonstrating an order to disorder transition. Figure 4.1 (c) shows diffraction pattern of disordered FCC structure with (001) zone axis at 550 °C. All oxidation experiments reported were performed above the T_C (=410 °C) to make the results comparable to the previously obtained Cu (001) oxidation.

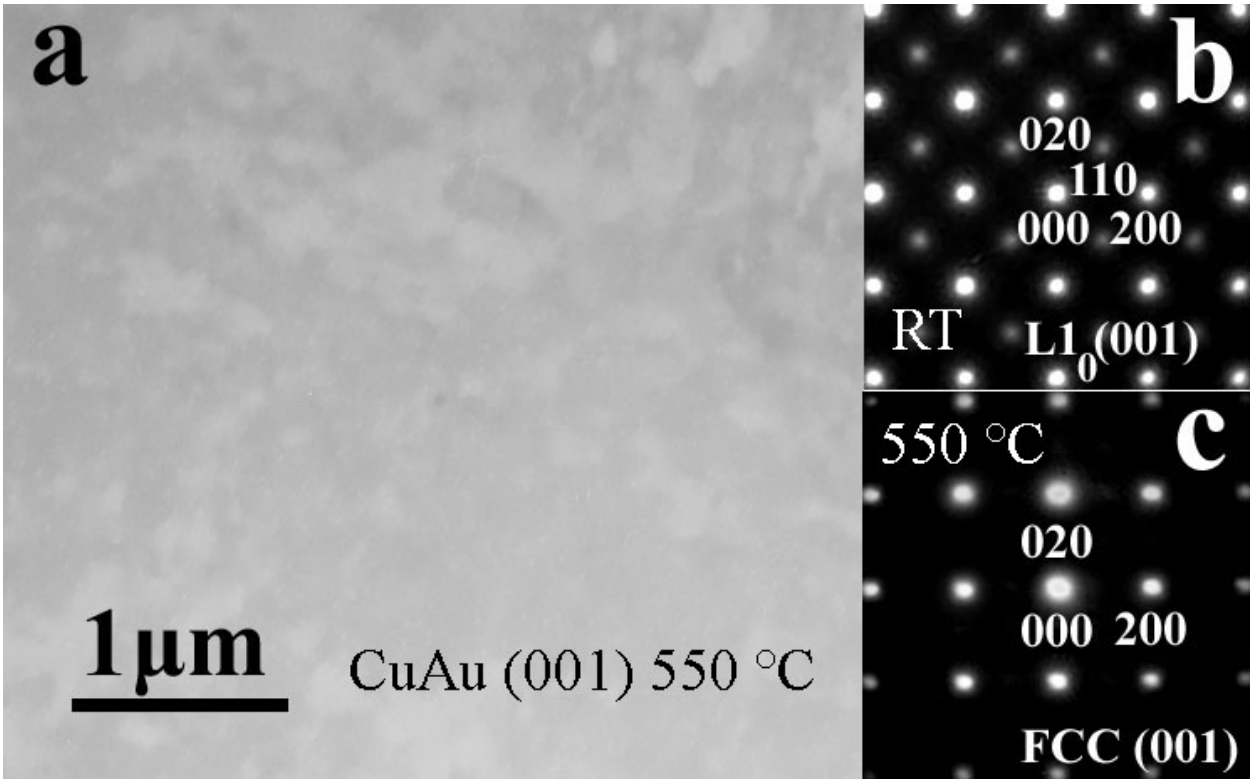

Figure 4.1 (a) BF TEM image of $Cu_{0.5}Au_{0.5}$ film at 550 °C, (b) diffraction pattern at room temperature, (c) diffraction pattern at 550 °C.

4.2 OXIDE NUCLEATION

After admitting oxygen gas, the nuclei appear after an incubation time (τ_0, time from oxygen admitting to the appearance of the first nucleus) ranging from tens of seconds to several minutes depending on oxygen pressure, reaction temperature and gold composition. It is generally accepted that, during this incubation time, O_2 molecules striking the film dissociate and O atoms diffuse on the surface [28]. We speculate that the clean $Cu_{1-x}Au_x$ surface is rich in Au (Section 1.4), it is relatively inert toward oxygen adsorption and dissociation especially at low

temperature when Au concentration on the surface is higher [24]. Previous investigations [24-26] demonstrate that oxygen adsorption and dissociation is accomplished by Cu outward diffusion to the top layer to form Cu-O bond and Au inward diffusion as driven by the greater affinity of O for Cu than for Au. Further exposure to O_2 increases O concentration on the surface. This O saturated overlayer will facilitate homogeneous nucleation of Cu_2O when the chemical potential of oxygen reaches a critical point (as determined by temperature, oxygen pressure and Cu concentration). Our experimental results show that, at the same oxygen partial pressure (5×10^{-4} torr), τ_0 decreases as temperature increases, e.g. T = 600 °C τ_0 = 4 min, T = 650 °C τ_0 = 3 min, and T = 700 °C τ_0 = 50 s. Compared with Cu (001) which has incubation times of 1.5 min for 600°C oxidation, 1 min for 650 °C, and <1 min for 700 °C <1 [64], $Cu_{0.5}Au_{0.5}$ (001) has longer incubation times. The longer incubation times could be due to oxygen chemisorption needing much longer time on the Cu-Au surface than on pure Cu, because it involves diffusion of both Cu and Au. As the temperature increases, the higher mobility of the atoms allows more rapid adsorption of oxygen and thus the incubation time shortens with increasing temperature.

After the first nucleus appears, the nuclei density increases with time until a saturation density is reached and then it will decrease as islands start to coalesce. The oxidation process can be characterized by an initial nucleation rate [30]. The initial nucleation rate is $dN/dt \propto \exp(E_{Des} - E_S - \Delta G^*)$ [31] where E_{Des}, E_S and ΔG^* are the desorption activation energy of oxygen atom from the surface, diffusion activation energy of oxygen atom on the surface, and Gibbs free energy change of forming a critical oxide nucleus (or activation energy for nucleation) respectively. As is discussed in Section 1.4, during oxide nucleation on Cu-Au, oxygen is diffusing on a Cu rich surface, so E_{Des} and E_S should have similar values as on pure Cu surface. Hence, faster initial nucleation rate corresponds to smaller ΔG^*. In $Cu_{0.5}Au_{0.5}$ the saturation

density is reached surprisingly fast. For example, at 550 °C and $P(O_2) = 5\times10^{-4}$ torr, the saturation density has been reached after only 30 seconds (which is roughly the time to advance a negative film plus exposure), thus an initial nucleation rate of 7.3 $\mu m^{-2}min^{-1}$ could be deduced. In comparison, the initial nucleation rates for Cu (100) and Cu (110) oxidation at 350 ºC are 0.17 μm^{-2} min^{-1} [65] and 1.74 μm^{-2} min^{-1} [28] respectively. In section 4.4 the energetics of nucleation will be discussed in detail.

4.3 MORPHOLOGY EVOLUTION

The primitive cell of Cu_2O is cubic with space group *Pn-3m* (*a*=4.22 Å), and contains two oxygen and four copper atoms. [66] The oxygen atoms form a body centered cubic structure, while the copper atoms partially occupy the interstitial positions in an alternating pattern. Figure 4.2 (a) shows typical shape of the Cu_2O oxidized at 600 °C. Island with a square base are clearly distinguished and there is a cross-shaped pattern suggesting the island probably has a pyramid shape. NED (Figure 4.2 (b)) was taken by ~100nm parallel electron beam illuminating only the oxide island. NED was utilized here instead of SAED (selected area electron diffraction) to reveal week diffraction from nanoarea oxide islands that would have been otherwise overshadowed by the strong diffraction from the metal substrate. Strong diffraction spots in Figure 4.2 (b) are those from the Cu-Au film. Associated with each strong spot are satellite diffractions from the oxide (see inset of Figure 4.2 (b)) which is characteristic of double diffraction. Since NED is done at room temperature, weak {110} superlattice reflections from the substrate also show up. The appearance of double diffraction demonstrates that the oxide island has not yet penetrated through the film. From the last two micrographs of Figure 4.2 (a),

an area with bright contrast appears at the center of the island. NED from only the central area (Figure 4.2 (c)) shows only Cu_2O diffraction spots that indicates penetration of oxide through the metal film when the island reaches a critical lateral size of ~200nm. Figure 4.2 also reveals several distinct configurations of the island. Cu_2O island grew with cube-on-cube crystallographic relationship to the film, i.e. Cu_2O (001)//$Cu_{0.5}Au_{0.5}$ (001) and Cu_2O [100]//$Cu_{0.5}Au_{0.5}$ [100]; the edges of Cu_2O pyramid before penetration are along <100> directions; after penetration the oxide maintains square-shape but the edges are now along <110> directions. Before penetration, the oxidation kinetics is comparable to bulk alloy oxidation and also the oxide grows in three dimensions. Furthermore, for all temperatures investigated in current thesis work, the same oxide morphology is observed.

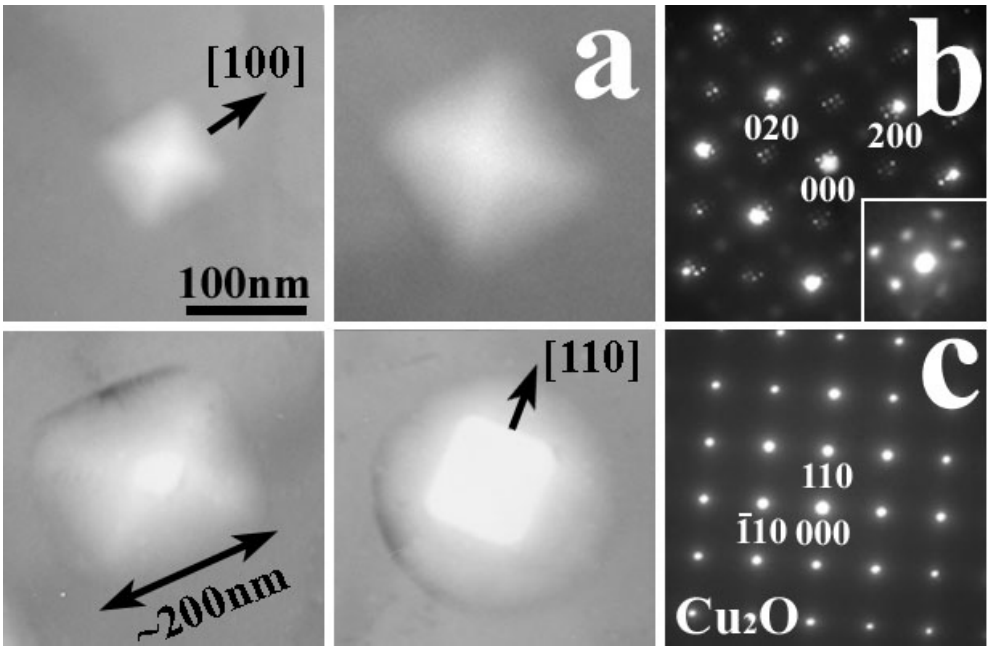

Figure 4.2 (a) shape evolution of an oxide island at 600 °C, (b) NED shows double diffraction from film and oxide, (c) NED from only Cu_2O

Unlike the triangular islands found in low temperature oxidation of Cu (001) (below 350 °C) [18, 65, 67] only square-shaped Cu_2O islands were observed in current research for all temperatures (from 550 to 750 °C). The reason probably is that the geometry of the island is the result of balance between surface/interface energy and strain energy. Since Cu_2O/Cu-Au alloy has much smaller lattice mismatch (10.5%) than that of Cu/Cu_2O (16.8%) which results in smaller strain energy. Previous work by Zhou *et al.*[19] reveals that strain can dramatically alter island morphology.

In order to determine the three dimensional shape of the island before penetration, we first use AFM to ascertain the topology of the Cu_2O island (Figure 4.3). Cross section height profiles passing through center (line scan #1) and off center (line scan #2) of the oxide island along the marked lines with <100> direction indicated in Figure 4.3 (a) are shown in Figure 4.3 (b) and (c) respectively. A triangular-shaped height profile through center plus trapezoid-shaped profile off center reveal the pyramid shape topology of the island. Figure 4.3 (b) and (c) also show that the four facets forming the pyramid have ~7° inclination angle to (001) film surface. Since these facets also intersect (001) plane at <100> direction, we have identified them as {108} plane.

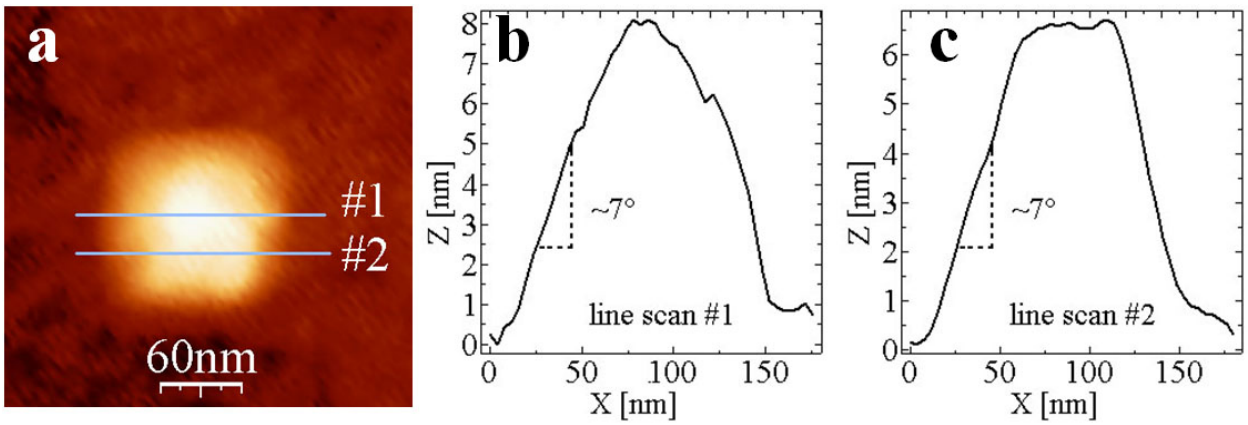

Figure 4.3 (a) Typical AFM image of the Cu_2O island, (b) line scan across the center and (c) off center. Both (b) and (c) show the inclination angle of the pyramid plane is around 7°.

Since the maximum size of the Cu_2O pyramid before penetration is ~200nm, and the film thickness is knows to be 90 nm, the crystallographic orientation of Cu_2O/Cu-Au could thus be inferred. As shown in the structure model of Figure 4.4 (a), the four interfaces form ~42° angle to (001) and they intersect (001) at <001> type directions. The only low index plane with these configurations is {110}. From the above analysis we determine the island shape before penetration to be an irregular-shaped octagon (Figure 4.4 (b)). The top of the octagon is enclosed by four {108} type facets and the Cu_2O facets at the Cu_2O/Cu-Au interfaces are {110} type. The volume of the island is $V = \frac{9}{48} l^3$ and projected area $A = l^2$, where l is the length of the base. This structural model demonstrates a 3D island growth mode before penetration.

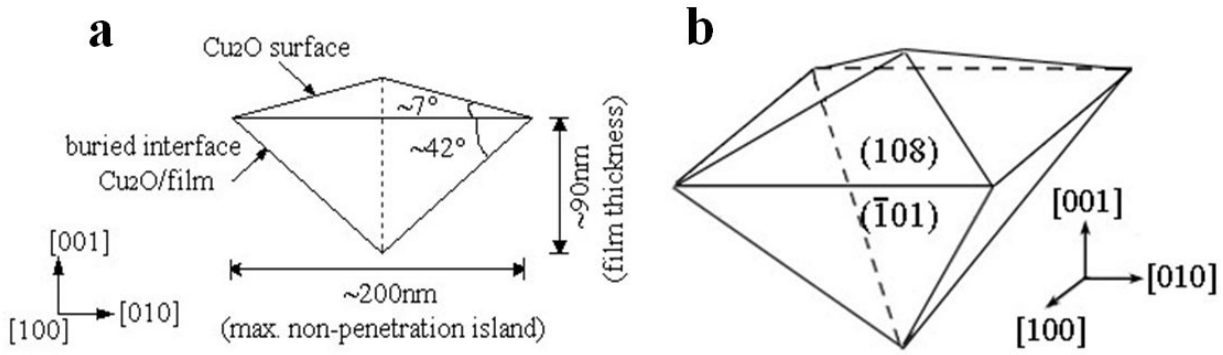

Figure 4.4 Structure model of Cu_2O islands. (a) two dimensional projection view from [100] direction; (b) projective view showing the irregular-shaped octagon structure.

One more interesting feature is the oxide shape evolution depicted by Figure 4.2. For islands smaller than ~200nm, their edges are along <100> directions. At about 200nm they "rotate" where <110> steps outgrew <100> steps and result in a seemingly 45° rotation to the original orientation. Figure 4.5 (a) is a typical AFM image with larger scan area. It shows that after penetration the islands continue growing with square-based shape and the island edges are along <110> direction. The islands that protrude out from the film are those nucleated on the top surface, while those indented areas corresponding to islands nucleated on the other surface. Figure 4.5 (b) shows the cross-section height profile of one island labeled in Figure 4.5 (a). The trapezoid cross sectional profile indicates that the island has flat top with (001) crystal plane while the other facets were indexed as {115} plane.

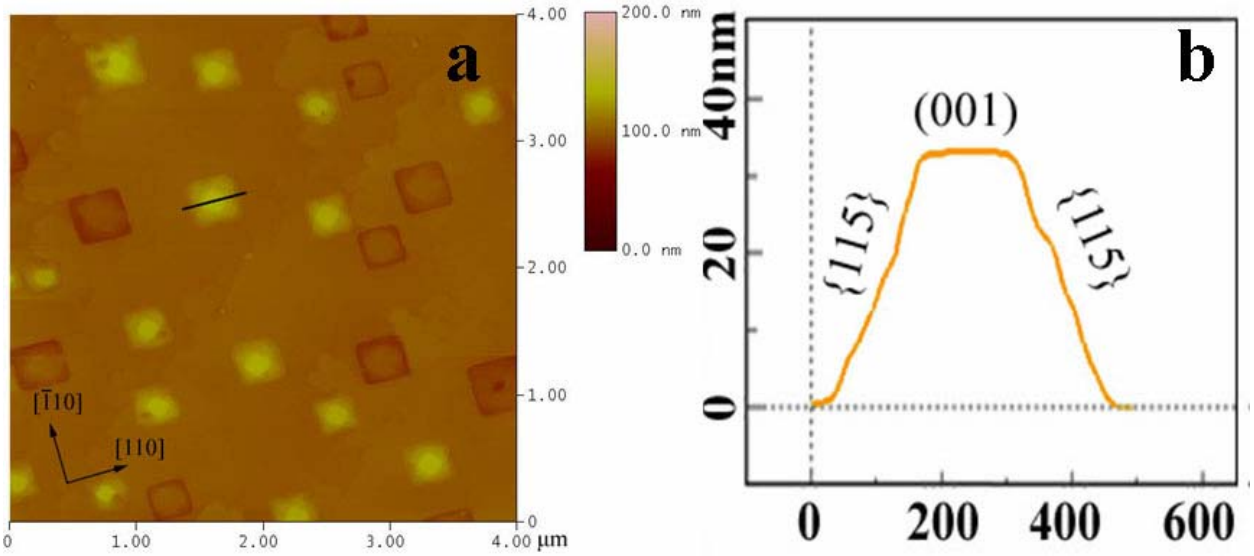

Figure 4.5 (a) typical AFM image of oxide islands after penetration, (b) height profile of one island.

Figures 4.6 shows the formation mechanism of the square-shaped indentation beneath each oxide island. First the island nucleates on the surface. As the island grows, it draws Cu atoms from the film. Surface Cu diffusion could be one major means for long-range Cu supply since it has smaller activation energy (ΔE_{bulk}=1.13 eV and $\Delta E_{surface}$=0.6 eV [68]). Although bulk diffusion requires more energy, Cu atoms beneath the Cu_2O/metal interface could still diffuse to the growing interface because of shorter diffusion length, thus creating the indentation. It also indicates that before penetration oxide island grows in 3D and after penetration oxide grows in 2D mode where the oxide thickness remains the same.

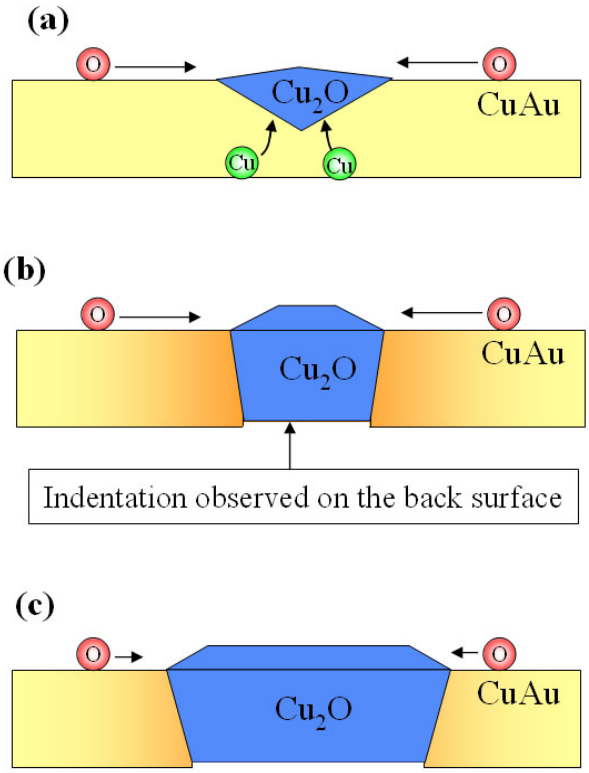

Figure 4.6 The formation mechanism of indentation beneath the island. (a) growing island consumes Cu beneath, (b) indentation created when Cu atoms are used up, (c) after penetration, the island grows in lateral direction while the thickness remains the same.

4.4 ENERGETICS OF NUCLEATION

The overall free energy for oxidation is determined by molar Gibbs free energy of formation of Cu_2O (ΔG^f), surface energy changes, and interfacial energy change in the oxide as

$$\Delta G = \Delta G^f \frac{V}{V_o} + (\gamma_o A_o - \gamma_m A_m + \gamma_{o/m} A_{o/m}) + \frac{E}{1-\nu}\varepsilon^2 V \qquad \text{Equation 4.1}$$

where V and V_o are the volume and molar volume of Cu_2O. γ_o, γ_m, and $\gamma_{o/m}$ are the surface energy of oxide, metal, and the chemical energy that arises from interfacial bonding [69]. A_o, A_m, and $A_{o/m}$ are areas of oxide, metal and Cu_2O/Cu-Au interface. The last term in Equation 4.1 is the elastic strain energy stored in the oxide due to lattice mismatch between Cu_2O and Cu-Au film. v and E denote Poisson's ratio and Young's modulus of Cu_2O, respectively. ε is the lattice mismatch of Cu_2O/Cu-Au and is defined as $\varepsilon=a_{\text{oxide}}-a_{\text{metal}}/a_{\text{metal}}$. The strain energy term is modified from the results by Jeurgens *et al.* [69]. In reference [69] the strain energy is proposed to be proportional to the thickness of the oxide layer that is strained. In current work, since the nucleus size is small (the smallest island that can be resolved by TEM is around one nanometer), it is assumed the whole oxide islands are strained, and thus the strain energy is proportional to island volume.

From classical nucleation theory we know that the critical nuclei size l^* and the Gibbs free energy change for forming critical nuclei ΔG^* are

$$l^* \propto -\frac{\Gamma}{\frac{\Delta G^f}{V_o}+\frac{E}{1-\nu}\varepsilon^2} \qquad \text{Equation 4.2}$$

and

$$\Delta G^* \propto \frac{\Gamma^3}{(\frac{\Delta G^f}{V_o}+\frac{E}{1-\nu}\varepsilon^2)^2} \qquad \text{Equation 4.3}$$

where Γ is the surface and interface energy term (here Γ is defined, so that $\Gamma l^2 = \gamma_o A_o - \gamma_m A_m + \gamma_{o/m} A_{o/m}$). In order to compare the nucleation energy of Cu_2O in Cu-Au alloy and that in Cu, a term by term comparison of Γ, $\Delta G^f / V_0$, and $\frac{E}{1-\nu}\varepsilon^2$ is needed. At present, experimental values of surface and interface energy of metal-oxide are usually not available, but

to a good approximation γ_m for Cu-Au surface is assumed to equal to γ_{Cu} because in both cases oxide nucleates on oxygen saturated Cu rich surface (see Section 1.4 for details). $\gamma_{o/m}$, the interfacial energy between oxide and Cu-Au is assumed to equal to that of oxide/Cu. This could be a valid assumption since metal/oxide interfacial energy should generally have similar value. Thus the problem could be simplified by comparing only $\Delta G^f / V_0$ term and $\frac{E}{1-\nu}\varepsilon^2$ term of Equation 4.2 and Equation 4.3.

Standard thermodynamic data [70] shows that

$$\Delta G^f = -166,500 + (122.2 - 16.63\ln[\mathrm{Cu}])T \qquad \text{Equation 4.4}$$

where [Cu] is the activity of copper. It equals to 1 for pure Cu and 0.5 in $Cu_{0.5}Au_{0.5}$ under ideal solution assumption. Then for Cu and $Cu_{0.5}Au_{0.5}$ alloy oxidation, it could be calculated that $(\Delta G^f / V_0)_{\mathrm{Cu}} = -1.19\times10^6\,\mathrm{KJ/m^3}$ and $(\Delta G^f / V_0)_{\mathrm{Cu_{0.5}Au_{0.5}}} = -0.95\times10^6\,\mathrm{KJ/m^3}$ respectively. It is thus apparent that the $\Delta G^f / V_0$ term for $Cu_{0.5}Au_{0.5}$ oxidation is less negative than that of pure Cu due to the reduced activity of Cu in $Cu_{0.5}Au_{0.5}$.

As to the elastic strain energy, the lattice mismatch between Cu_2O and Cu is 16.8%, while in $Cu_{0.5}Au_{0.5}$ ε=10.5% ($a_{\mathrm{Cu_2O}}$=4.22 Å, a_{Cu}=3.61 Å, a_{Au} = 4.02 Å and by Vegard's law $a_{\mathrm{Cu_{0.5}Au_{0.5}}}$ = 3.82 Å). Substituting the value of ν (=0.455) and E (=30GPa) of Cu_2O [71], we have $(\frac{E}{1-\nu}\varepsilon^2)_{\mathrm{Cu_2O/Cu}} = 1.55\times10^6\,\mathrm{KJ/m^3}$ and $(\frac{E}{1-\nu}\varepsilon^2)_{\mathrm{Cu_2O/Cu_{0.5}Au_{0.5}}} = 0.61\times10^6\,\mathrm{KJ/m^3}$. Hence, by adding Au into the system, the lattice mismatch induced strain energy is reduced.

To summarize, the dominant effect of Au to ΔG is two fold; first, it increases ΔG by reducing Cu activity and thus increase Gibbs free energy for Cu_2O formation and hinders nucleation; secondly, it reduces the elastic strain energy and enhances nucleation. These two effects make

opposite contribution to the overall Gibbs free energy change, i.e. change in ΔG^f increases ΔG and better lattice match of Cu_2O/Cu-Au decreases ΔG. The net effect is the combination of the two. Since $Cu_{0.5}Au_{0.5}$ has a much faster nucleation rate, it means the overall Gibbs free energy is lower than that of Cu (001). Hence $\frac{E}{1-\nu}\varepsilon^2$ term contributes more to the overall Gibbs energy change. Accordingly lower energy for oxide nucleation results. In section 4.2 it is mentioned that $Cu_{0.5}Au_{0.5}$ oxidation shows a surprisingly fast nucleation rate as compared to that of Cu oxidation. The above energetics argument predicts the exact behavior that we observed. Since nucleation rate is proportional to $\exp(-\Delta G^*/kT)$, decreases in ΔG^* dramatically increase the nucleation rate so that we could not record any nucleation event.

Schematically, the Gibbs free energy change as a function of particle size in Equation 4.1 is plotted in Figure 4.7. Solid lines are those for Cu oxidation and dotted lines are for $Cu_{0.5}Au_{0.5}$ oxidation. Notice that $(\frac{\Delta G^f}{V_o}+\frac{E}{1-\nu}\varepsilon^2)l^3$ is more negative in the case of $Cu_{0.5}Au_{0.5}$ which makes both ΔG^* and l^* smaller.

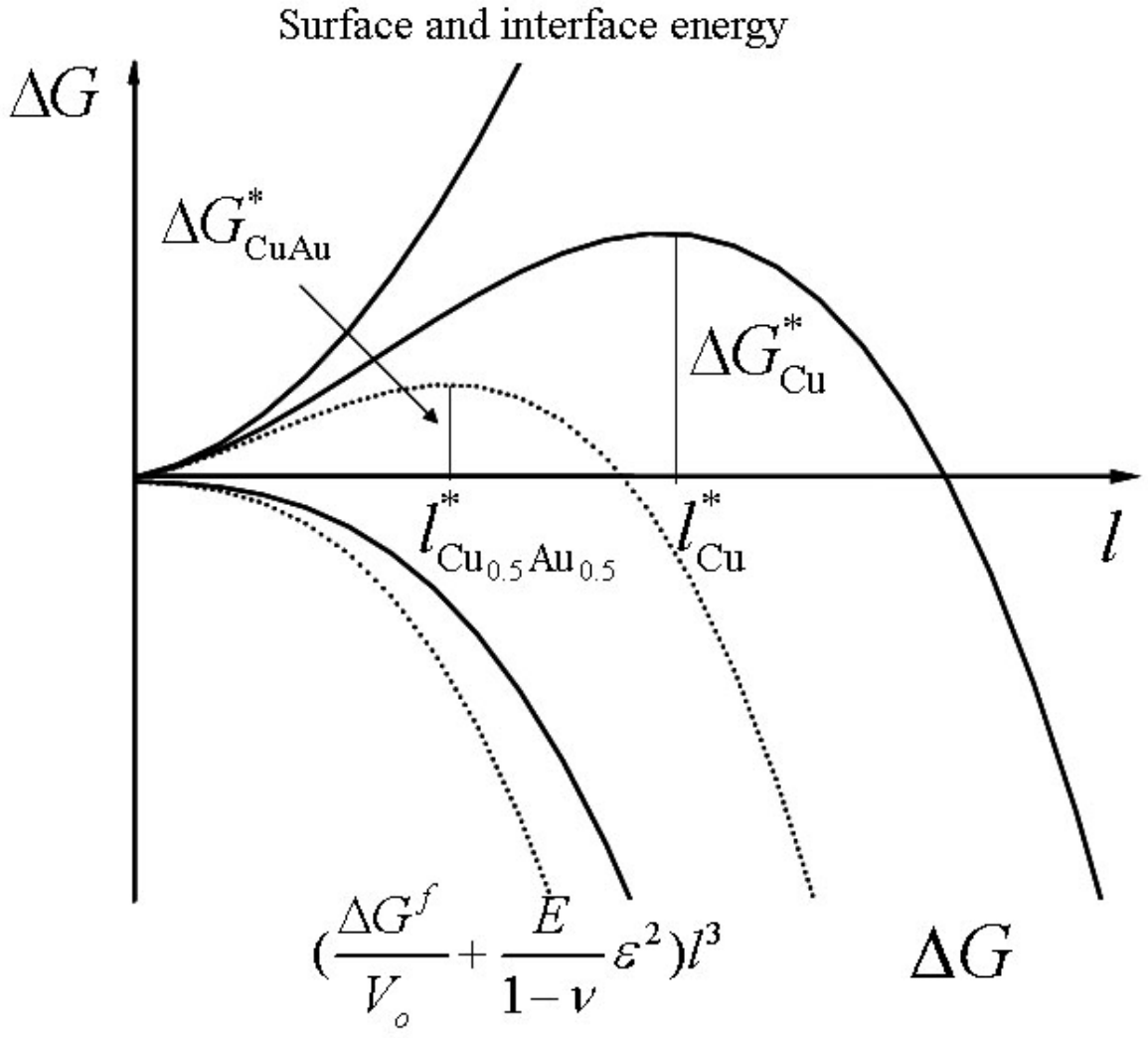

Figure 4.7 Gibbs free energy change as a function of nuclei size. Cu-Au oxidation has smaller critical nuclei size and activation energy for nucleation.

As is discussed in section 1.2.2, the saturation island density dependence on reaction temperature follows an Arrhenius relationship [31]

$$N_S \propto \exp(-\Delta G^* / kT) \qquad \text{Equation 4.5}$$

We measured the saturation density of the nuclei as a function of oxidation temperature, from 550 to 700 ºC with $P(O_2)=5\times10^{-4}$ torr. Figure 4.8 shows the Arrhenius plot. The activation energy (or Gibbs free energy change for critical nucleus formation), ΔG^*, which is equal to the slope, iss determined to be 0.9±0.1 eV. In comparison, the Arrehnius plot for previous work on Cu (001) oxidation [65] from 290 – 435 °C is also shown in the same figure. Cu (001) oxidation has an activation energy of 1.4±0.2 eV which is higher than that of $Cu_{0.5}Au_{0.5}$ suggesting a consistency with above analysis.

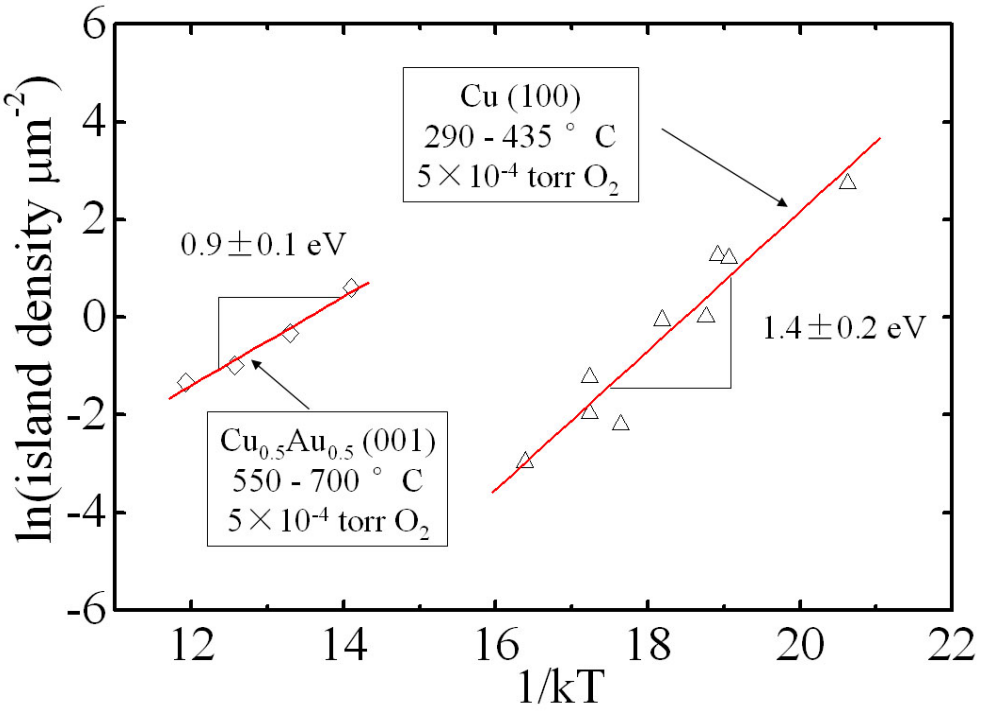

Figure 4.8 Arrenhius plots for current research and previous works on Cu (001) [65] oxidation.

4.5 OXIDE GROWTH KINETICS

Since Au does not form stable oxide under current conditions, and is not soluble in Cu_2O, the oxidation of Cu-Au alloys results in the rejection of Au, leading to Au enrichment in the metal/oxide boundary. Figure 4.9 (a) is a STEM Z-contrast image of an oxide island formed on Cu38%Au (001) surface at 700 °C and 5×10^{-4} torr oxygen pressure for 30 min. Figure 4.9 (b), and Figure 4.9 (c) show the corresponding EDS oxygen and gold elemental map. Bright contrast around the island in both Z-contrast image and EDS gold map demonstrate a 300-500 nm wide Au-rich region around the Cu_2O island. Therefore, the growth of the oxide islands in the oxidation of Cu-Au alloys involves the diffusion of oxygen, Cu and Au atoms. Hence, unlike the linear oxide growth kinetics found in pure oxidation where oxygen surface diffusion alone limits the whole process, the growth of Cu_2O islands on $Cu_{0.5}Au_{0.5}$ alloy could be determined by either oxygen surface diffusion or Cu supply or even both. Two oxide growth regimes could be separated, namely, the initial 3D growth regime and the self-limiting 2D growth regime. At the very initial stage of oxide growth there is no significant segregation of Au, thus growth rate is dominated by oxygen surface diffusion. As reaction proceeds, the Au build-up zone gets thicker and inhibits Cu diffusion through this Au rich layer until the growth finally stops. In Figure 4.9 (a), the Au rich region has a sharp boundary. It could possibly due to Au segregation to the film surface and form a step like region. Further analysis such AFM is needed to elucidate the reason for the step-like structure.

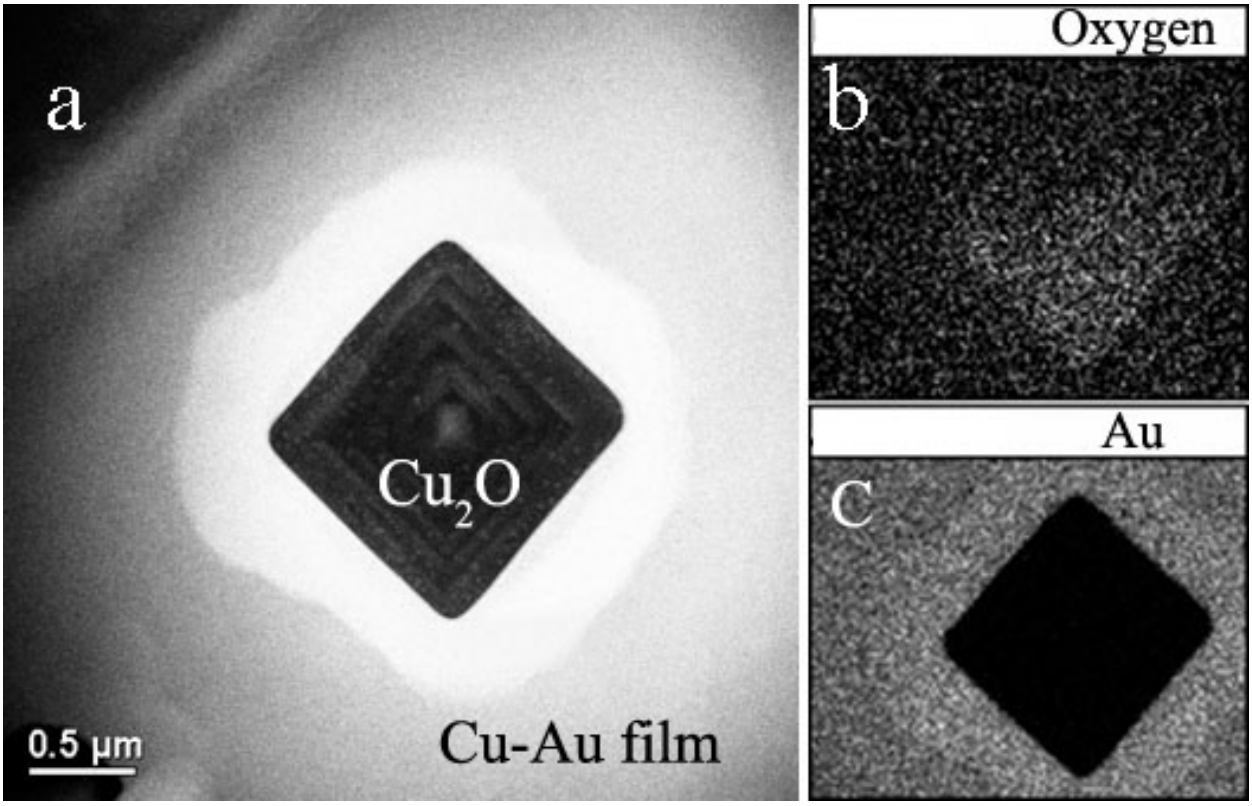

Figure 4.9 (a) STEM Z-contrast image and EDS elemental map for (b) oxygen and (c) gold.

4.5.1 Initial Linear Oxide Growth Kinetics

As is shown in Figure 4.6, there are two modes of island growth, namely, 3D growth before penetration and 2D growth after. In this section, the initial 3D growth regime will be discussed. The oxide growth kinetics is characterized by the increase in cross sectional area versus oxidation time. It is phenomenologically described in classical mean-field theory that the growth of surface features follow scaling law such that [18, 72, 73]

$$A(t) = G(t - t_0)^n \qquad \text{Equation 4.6}$$

where G is the area growth factor; t_0 is the time at which island nucleates; t is lapse of time from oxygen exposure; and n is the power law dependence. Yang *et al.* [18] demonstrates that for 3D island growth, n equals to 1, while for 2D island growth, n is 2 if surface oxygen diffusion is the major transport mechanism. As has been discussed in Section 3.4, before penetration Cu_2O islands assume 3D growth mode. Figure 4.10 (a)-(c) depict three typical TEM images of island growth at 650 °C. The images were acquired at times t = 5 min, 10 min and 17 min. In Figure 4.10 (c), island 3 already penetrated through the film revealed by the characteristic white contrast in the center. An excellent fit of experimental data to linear growth law was obtained in Figure 4.10 (d), where the average cross-sectional area of the oxide as a function of reaction time is plotted; G=0.00255 ± 0.00004 μm^2/min, t_0=2.3 ± 0.1 min and the goodness of fitting R=0.999. The initial growth behavior of the oxides at other temperatures (e.g. 550 °C, 600 °C, 700 °C and 750 °C) follow the same linear power law dependence but with different G (e.g. G=0.06787 ±0.00345 μm^2/min and 0.0005 ± 0.0002 μm^2/min for 700 °C and 600 °C oxidation respectively). Generally, as the temperature increases, G also increases. The area growth factor G at 600 °C could be converted to volume growth factor as G'=2.1×10^3 nm^3/min. The volume growth factor for Cu (001) oxidation at 600 °C [17] is 1.2×10^5 nm^3/min which is almost two magnitudes larger than current result. Hence, introduction of gold suppresses the growth kinetic of Cu_2O.

The reduced oxidation kinetics in the initial stage of $Cu_{1-x}Au_x$ alloy oxidation can be explained by the fact that in Cu (001) oxidation there is no need for long-range Cu transportation, so oxygen surface diffusion controls the reaction. In Cu-Au oxidation, diffusion of Cu in Cu-Au alloy has an activation energy of ~1.6 eV [74, 75] and is the rate controlling mechanism. In fact, as revealed by Figure 4.9, in the later stage of oxidation, Au atoms partition out from the reaction interface and form a build-up layer in front of the Cu_2O/Cu-Au interface. This Au build-up layer

limits further supply of Cu to the reaction front and leads to a self-limited growth behavior (see next section).

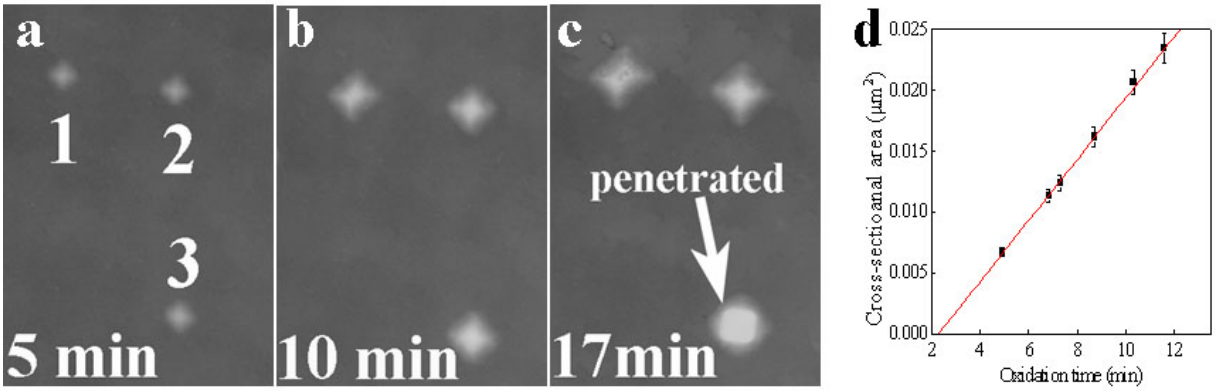

Figure 4.10 Typical BF TEM images of $Cu_{0.5}Au_{0.5}$ oxidation at 650 °C at (a) t = 5 min, (b) t = 10 min (c) t = 17 min as well as (d) linear fit to average cross section area vs. t.

4.5.2 Self-limiting Growth Kinetics

In this section, 2D growth mode after oxide penetrates through the film will be discussed. Figure 4.11 depicts the island growth as a function of reaction time at 700 ºC and $P(O_2)=5\times10^{-4}$ torr. After ~10 min reaction, the islands already penetrate through the film so their edges are along [110] directions. The dark contrast around growing islands circled in the third micrograph is the Au build-up zone. It is also seen that the growth of each island is determined by its own environment. For example, island 1 has largest inter-island spacing from its neighbor, i.e. largest denuded zone, thus it has more access to both oxygen and copper. This is why it grows into the largest island in the micrograph. The result means that although the mean-field theory can

predict the average behavior of all islands it can not be used to describe the individual island size evolution. Figure 4.12 (a) plots the cross section area of the four islands labeled in Figure 4.11 vs. reaction time. Although different islands have different sizes, they all follow similar growth pattern. Initially, all islands have a fast growth rate (d*A*/d*t*), and gradually, the islands grow slower and slower until they finally stop growing. If the island sizes are normalized by their maximum sizes (which is plotted in figure 4.12 (b)), all islands show exactly the same self-limiting growth behavior. Furthermore, similar self-limiting growth behavior was observed in $Cu_{0.5}Au_{0.5}$ (001) oxidation at 550 ºC, 600 ºC and 650 ºC suggesting its generality for Cu50at%Au alloy oxidation.

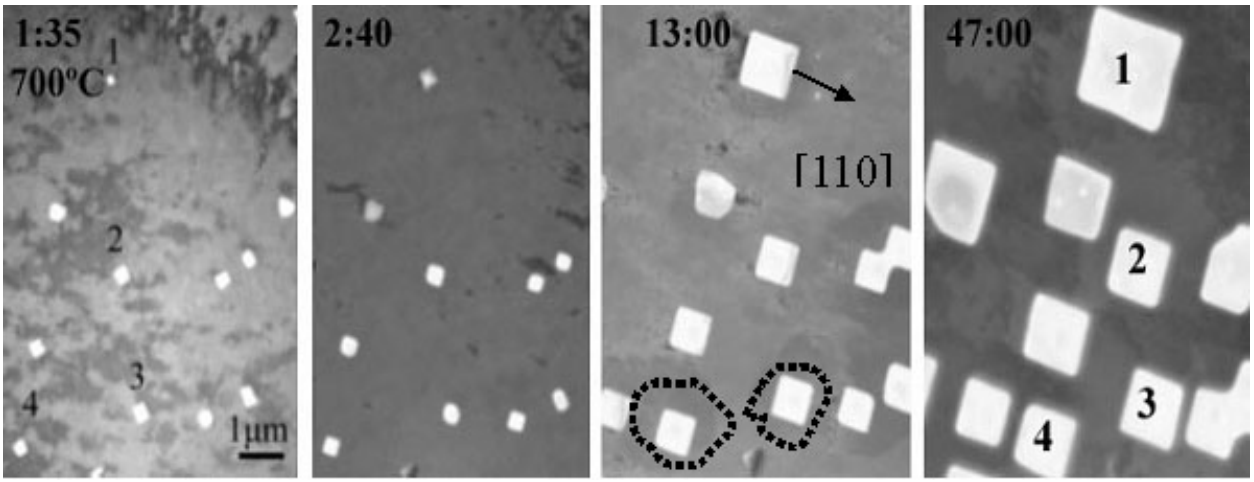

Figure 4.11 *In situ* bright field TEM image showing the growth of Cu_2O islands at 700 ºC.

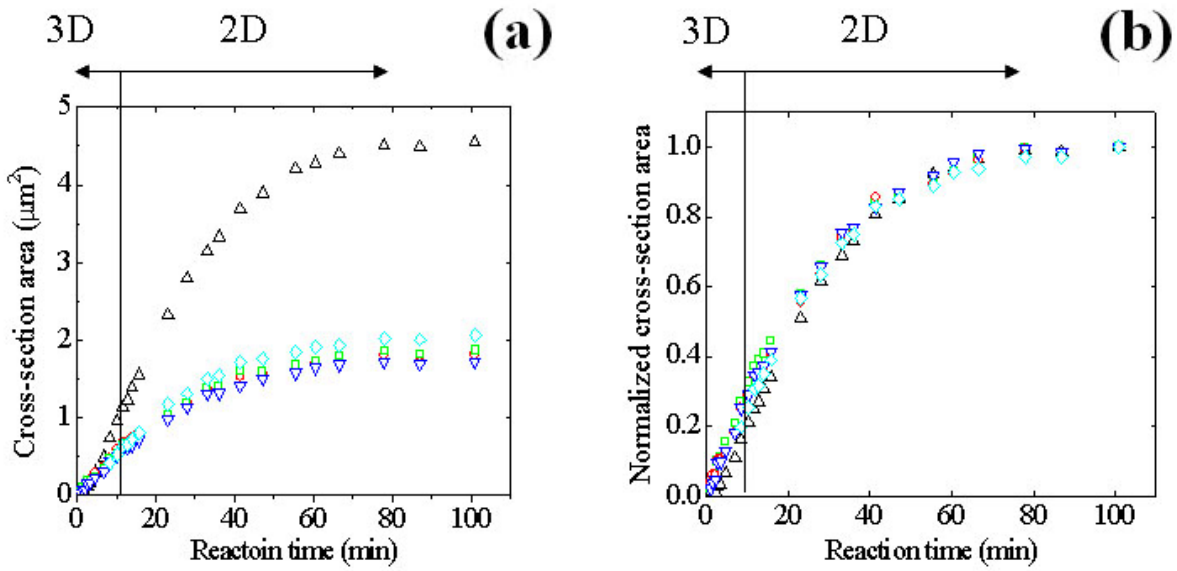

Figure 4.12 Plot of cross section area vs. reaction time for oxidation at 700 ºC showing self-limited growth behavior. (a) growth of the four islands labeled in Figure 4.11, (b) normalized cross-section area vs. reaction time for the four islands. The transition from 3D growth to 2D growth is also indicated.

On common way of solving island growth problem is first divide the surface into sub-regions (or cells). Only one growing island exists in one cell. The cell is called capture zone where the island inside draws atoms only from its own cell and the atoms out side the capture zone contributes to neighboring islands. Since there is no other island exists in the same cell, it is also called denuded zone. The size and shape of the capture zone is determined by inter-island spacing and position. In the 2D growth regime, the cell structure does not change, since there is no island nucleation (saturation density already achieved) and no coalescence. As shown in Figure 4.13, we first assume both the capture zone and the oxide island have circular shape with diameters of

2*R* and 2*r* respectively. Although the shape of the capture zone is irregular polygon and the oxide is square, this simplification should not damage the validity of the deduced model. Note that the capture zone size, *R*, is fixed while the oxide island size, *r*, increases with time.

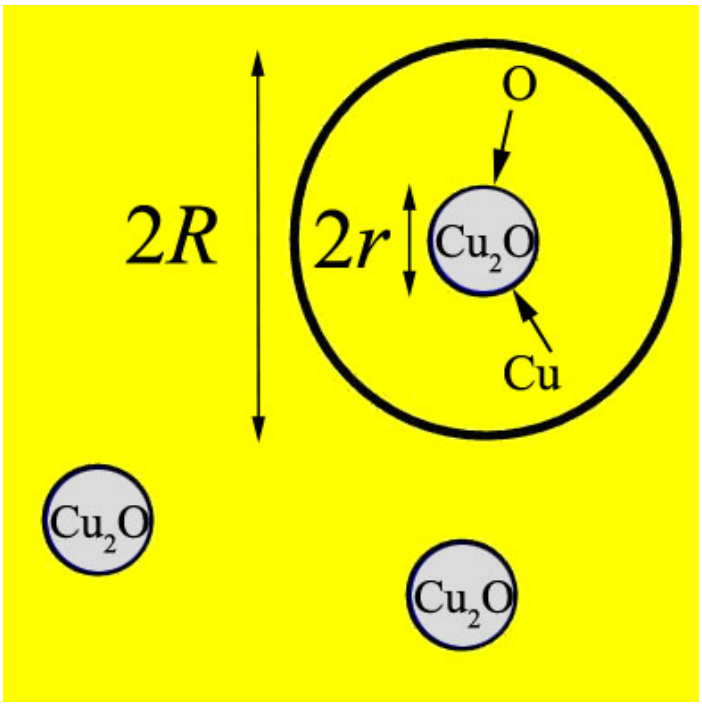

Figure 4.13 Schematic of the oxide islands and capture zone. Growing islands draw copper and oxygen only from the capture zone. 2*R* is the diameter of the capture zone and 2*r* is the diameter of the oxide.

The growth rate of the island is proportional to 1) Cu_2O/Cu-Au interface area where atoms incorporate into the island and 2) flux of copper to the island. The flux changes with time and is proportional to the total number of copper in the unreacted area of the capture zone times copper sticking coefficient. Thus the volume growth rate could be written as

$$\frac{dV(t)}{dt} = 2\pi r(t) h_{\mathrm{m}} \cdot \Omega_{\mathrm{o}} \cdot C_s f_s \frac{C(t)}{C(0)}, \qquad \text{Equation 4.7}$$

where *V(t)* is the volume of oxide at time *t*. *r(t)* is the island radius which is a function of time. $2\pi r(t)$ is the island perimeter. h_{m} is the thickness of the film and $2\pi r(t) \cdot h_{\mathrm{m}}$ gives the interface area between oxide and Cu-Au film. Ω_{o} is the volume per Cu atom in Cu_2O (which is the Cu_2O unit cell volume divided by the number of Cu atoms in one unit cell). Since the lattice constant of Cu_2O is 4.22 Å and there are 4 copper atoms in each unit cell, Ω_{o} could be calculated to be 1.88×10^{-11} μm^3. C_s is sticking coefficient of Cu to the oxide perimeter. f_s is copper flux at t=0. *C(t)* is the number of copper atoms left in the capture zone which equals to the total amount of Cu minus that already incorporated in the oxide. $f_{\mathrm{s}} C(t)/C(0)$ gives copper flux at time *t*. *C(t)* is given by:

$$C(t) = h_{\mathrm{m}} \cdot \pi R^2 / \Omega_{\mathrm{m}} - h_{\mathrm{o}} \cdot \pi r(t)^2 / \Omega_{\mathrm{o}} \qquad \text{Equation 4.8}$$

where h_{o} is the thickness of oxide. Ω_{m} is the volume in Cu-Au alloy occupied by one Cu atom. Similar to Ω_{o}, Ω_{m} has a value of 3.25×10^{-11} μm^3. $\pi R^2/\Omega_{\mathrm{m}}$ and $\pi r(t)^2/\Omega_{\mathrm{o}}$ give the total amount of copper atoms in the capture zone and that in the oxide respectively. *C(t)* decreases as *r(t)* increases since fewer copper atoms are available.

Since $V(t) = A(t) \cdot h_{\mathrm{o}} = 2\pi r^2(t) \cdot h_{\mathrm{o}}$ and h_{o}, the island thickness, is constant for 2D growth, Equation 4.7 could be rewritten as

$$\frac{dr(t)}{dt} = K_1 \cdot R^2 - K_2 \cdot r(t)^2, \qquad \text{Equation 4.9}$$

where $K_1 = \frac{\pi h_m^2 \Omega_{\mathrm{O}} C_s f_s}{2 h_{\mathrm{o}} \Omega_{\mathrm{m}} C(0)}$ and $K_2 = \frac{\pi h_m C_s f_s}{2C(0)}$ are constants. Integration gives

$$r(t) = R\sqrt{K_1/K_2}\,\mathrm{Tanh}(R\sqrt{K_1 K_2} \cdot t + C) \qquad \text{Equation 4.10}$$

where C is the integration constant. Thus $A(t)$ is

$$A(t) = \pi R^2 (K_1 / K_2) \mathrm{Tanh}^2 (R\sqrt{K_1 K_2} \cdot t + C) . \qquad \text{Equation 4.11}$$

By fitting to experimental data (see Figure 4.14), the parameters are determined as follows $\pi R^2 (K_1 / K_2)$ = 2.50598 ± 0.01342 μm^2, $R\sqrt{K_1 K_2}$ = 0.02944 ± 0.0007 min^{-1}, C = 0.26082 ± 0.01297 and the goodness of fitting is 0.99888. The fitting results for initial 3D growth and 2D self-limited growth is shown in Figure 4.14, where the symbols are experimental data of average island size for 700 ºC oxidation, solid line is the fitting to Equation 4.10 for reaction from 11.6 min to 101 min (i.e. 2D growth regime after oxide growth penetrates the film), and the dotted line is the linear fitting to Equation 4.6. The fitting parameters for this regime is G = 0.06787 ± 0.00345 μm^2 / min). As can be seen, Equation 4.10 describes the self-limiting behavior in the later stage of oxidation very well. On the other hand, the initial reaction regime can be perfectly described by linear growth model suggesting the transition from oxygen surface diffusion dominated growth mode to Cu supply determined growth mode.

Since $\pi R^2 (K_1 / K_2)$ and $R\sqrt{K_1 K_2}$ terms are known, and the experimental value for R is 0.288 μm, K_1 and K_2 could be solved to be 0.317005 μm^{-1} min^{-1} and 0.0329628 μm^{-1} min^{-1} respectively. Then $C_s f_s$ could be calculated to be around 1.7×10^8 μm^{-2} min^{-1} or 2.8×10^7 μm^{-2} s^{-1}. The exact solution for C_s and f_s is not accessible from current results only. But if the system is assumed to be far from equilibrium and $C_s \approx 1$, then the initial copper flux is estimated to be 2.8×10^7 μm^{-2} s^{-1}. Let Equation 4.6 equals to Equation 4.11, the exact time of 3D to 2D transition is solved to be at t=10.5 min which agrees well with the experimental observation.

This model describing the self-limiting growth of oxide assumes that oxidation of Cu is not reversible, so there is no dissociation term in Equation 4.7. Actually from Equation 4.8 the island stops growing only when $C(t)$ is zero, i.e. all Cu atoms in the capture zone are oxidized. This is

not true since when oxide stops growing certain amount of Cu need to present in the film to maintain local equilibrium.

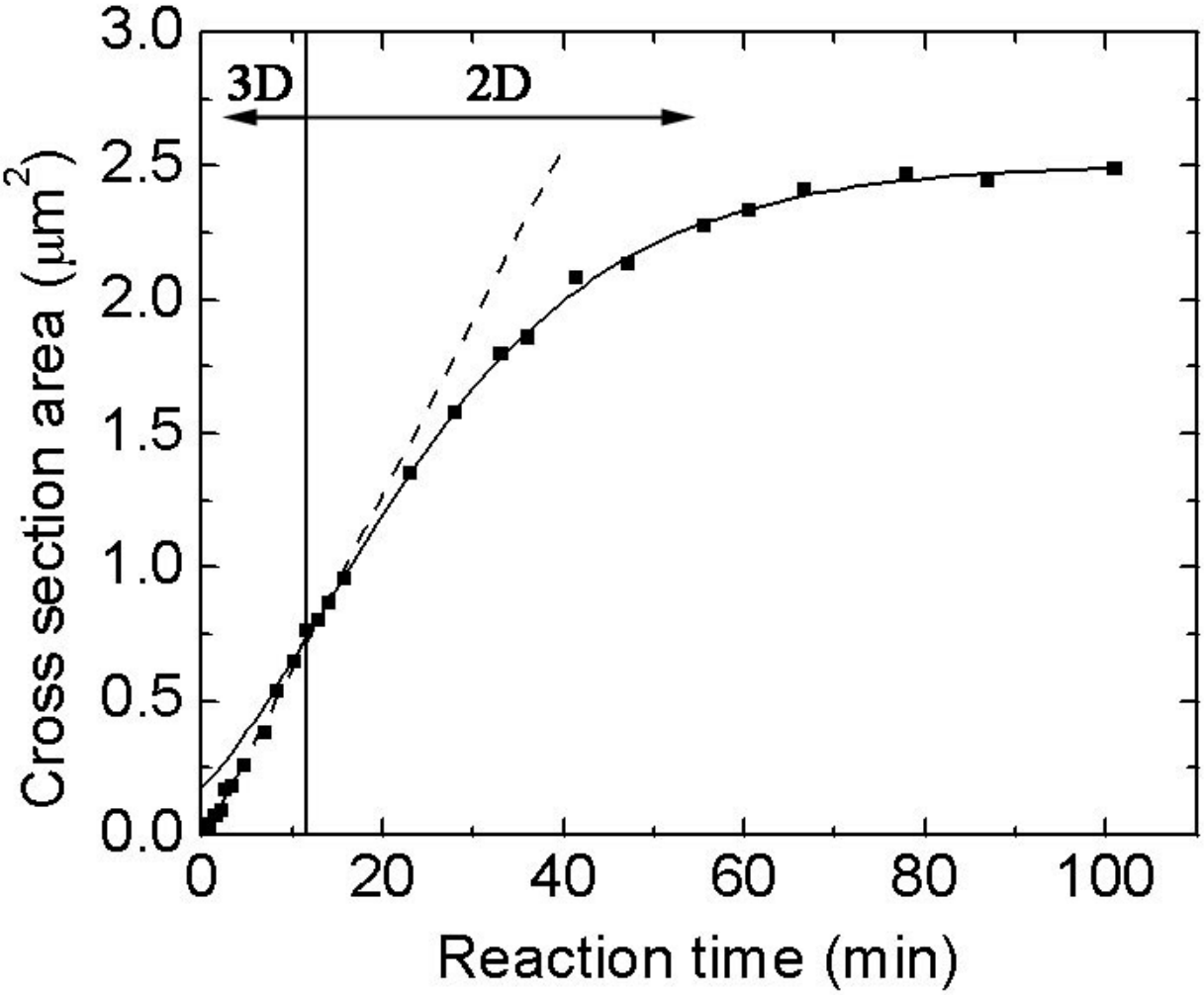

Figure 4.14 Fitting of experimental data to linear growth law and self-limiting growth law.

The reasons why islands stop growing after long time oxygen exposure could be either kinetics limited or energetics limited. If it is kinetically limited then ideally there should be no Cu concentration gradient across the unoxidized film since any concentration gradient will lead to

further diffuse of Cu and thus further grow of the islands. Experimentally (Figure 4.9), there still exists a concentration gradient even when the islands stop growing. So we think that a local equilibrium might have been established at the interface of $Cu_{0.5}Au_{0.5}/Cu_2O$ at the given temperature and oxygen pressure, since it is possible that the interface could have high level of Au segregation.

The results of oxide growth kinetics indicate that when gold is added to the system it suppress the growth of the islands. The apparent activation energy for island growth E_G, can be obtained by considering the Arrhenius dependence of growth rate R on reaction temperature, i.e. $R \sim \exp(-E_G / kT)$. Research on other concentration of Au shows that, at the same temperature range, E_G increases as gold concentration increases also suggesting the suppression effect of gold on reaction kinetics [76]. Table 4.1 lists the nucleation activation energy (ΔG^*) and the apparent oxide growth activation energy (E_G, which is obtained for Cu-Au films with different composition from the Arrhenius plot of initial oxide growth rate as a function of reaction temperature).

Table 4.1 Comparison of the activation energies (ΔG^*) for nucleation of the oxide island and the apparent oxide growth activation energy (E_G) for oxide growth in oxidation of the Cu-Au alloys with different Au mole fraction (C_{Au}). [76]

C_{Au} [30]	0.00	0.05	0.10	0.15	0.20	0.38
ΔG^*	1.4±0.2	1.11±0.1	1.01±0.1	0.96±0.1	0.93±0.1	0.91±0.1
E_G		0.97±0.1	1.07±0.1	1.15±0.1	1.19±0.1	1.3±0.1

The above table reveals that the nucleation energy decreases as Au concentration increases, i.e. the addition of Au to the alloy enhances nucleation of Cu_2O. On the other hand, as gold concentration increases, the activation energy for oxide growth decreases, i.e. addition of gold suppresses oxide growth.

5.0 CONCLUSIONS

The initial stages of oxidation of $Cu_{0.5}Au_{0.5}$ (000) single crystal alloy thin films at the temperature from 550 to 700 ºC with oxygen partial pressure of 5×10^{-4} torr have been investigated by *in situ* UHV-TEM to model the nano-oxidation of alloys with one active component and one nonoxidizing component. It is demonstrated that the addition of gold has a dramatic effect on the kinetics and energetics of oxide nucleation and growth. Similar to that of Cu (001) oxidation, square-shaped Cu_2O islands with cube-on-cube crystallographic orientation relationship were formed. In $Cu_{1-x}Au_x$ alloy, the segregation of gold to the surface leads to a longer nucleation incubation time compared to Cu oxidation at the same condition. Both experiment and quantitative analysis show that the addition of Au also enhances the oxide nucleation by reducing the elastic strain energy. Two regimes of oxide growth were observed. Initially, the growth was limited by oxygen surface diffusion which has a linear dependence on time. As the oxide continues to grow, gold builds up at the metal/oxide interface. This Au build-up zone inhibits further diffusion of copper atoms and leads to a self-limiting growth behavior. A model is proposed to quantitatively describe the self-limiting oxide growth.

6.0 FUTURE WORKS

This work has demonstrated the significantly different oxidation behavior of $Cu_{0.5}Au_{0.5}$ alloy with Cu, such as enhanced nucleation, suppressed growth rate and self-limiting growth mode. Nevertheless, to gain systematic understanding of inert gold on the initial oxidation behavior of Cu, further work on oxidation of alloy films with different orientation and alloy concentration at different temperature and oxygen pressure should be included. It is expected that combination of gold concentration, oxygen partial pressure and temperature may alter reaction energetics and kinetics significantly, thus leading to more complicated and interesting phenomena.

One example is the fractal growth of Cu_2O island of Cu15at%Au (001) oxidation at 600 ºC with $P(O_2)=5\times10^{-4}$ torr shown in Figure 6.1. At this reaction condition, the island initially has a compact shape. When its size reaches ~800nm, the island starts to show a fractal shape. Detailed reason for this transition is still being investigated.

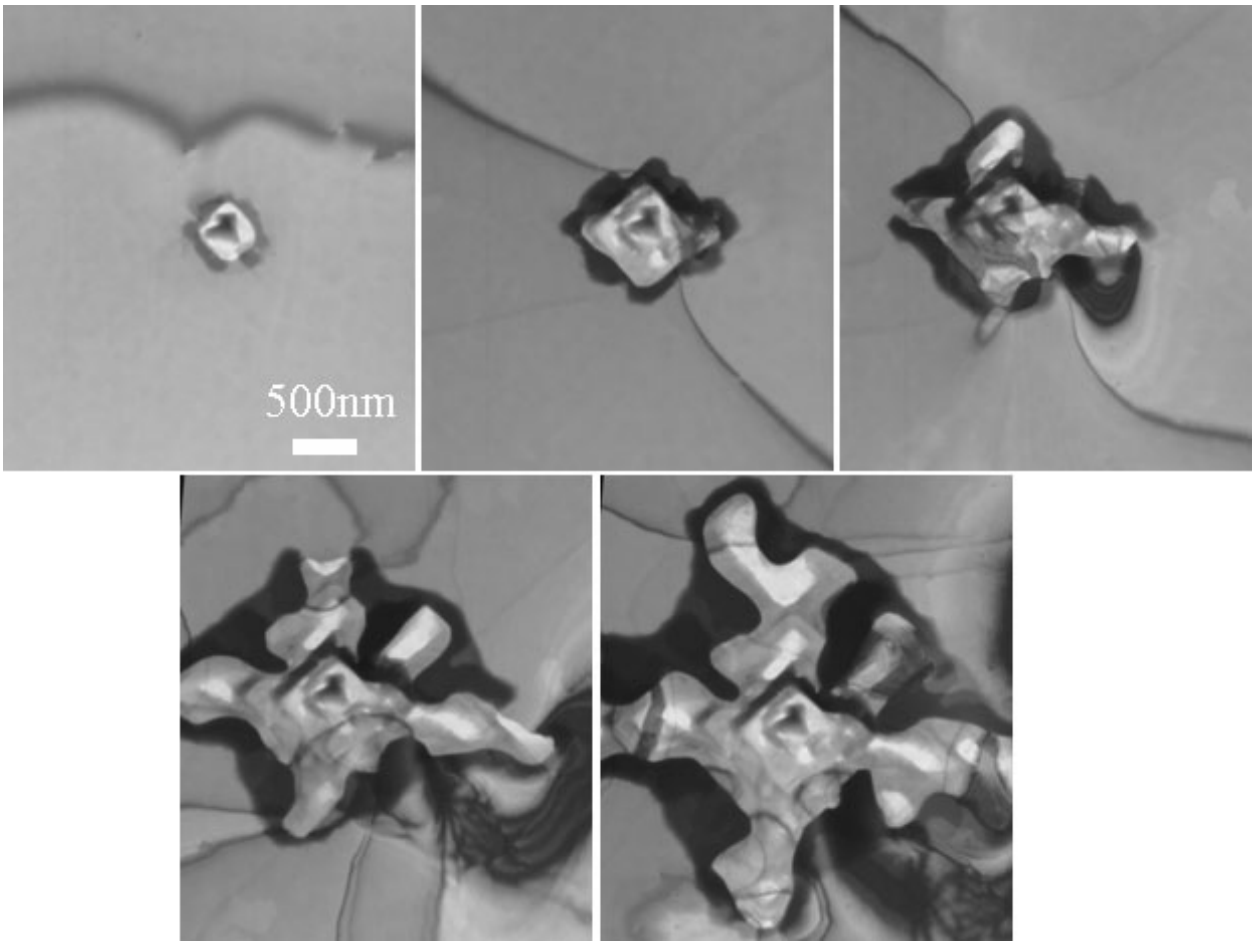

Figure 6.1 *In situ* observation of the oxide island growth at 600 ºC on Cu15at%Au (001). A transition from initially compact to fractal shape is revealed.

In the meantime, since the morphology of the oxide island is controlled by the competition between interfacial strain energy and surface energy, detailed investigation of metal/oxide interface structure (such as cross section TEM) would give more information in elucidating the morphology evolution.

Although *in situ* UHV-TEM provides a powerful tool in revealing the dynamic process of alloy oxidation, there are still information remains inaccessible by only TEM. For example, TEM can

only see the projected structure along electron beam path. Thus issues like the metal/oxide interface structure, detailed atomistic level information of Cu, Au, and O transportation at the very initial stages, strain distribution in and around the oxide, bonding state change of oxygen, to name a few, that are so critical to initial oxidation can be obtained only by means other than TEM.

Furthermore, computer simulation of heteroepitaxial oxide growth (e.g. Kinetic Monte Carlo, KMC) could serve as a complimentary tool for TEM.

Since Au does not oxidize at current condition, Cu-Au alloy represents the simplest alloy system. The real engineering materials may contain several active constituents. Alloys with more than one active component such as Cu-Ni, Ni-Al, Fe-Ni, etc. should also be included in future research.

BIBLIOGRAPHY

1. P. Marikar, M.B. Brodsky, C.H. Sowers, and N.J. Zaluzec: Insitu Hvem Studies of the Early Stages of Oxidation of Nickel and Nickel Chromium-Alloys. *Ultramicroscopy.* **29**, 247 (1989).

2. P.H. Holloway, and J.B. Hudson: Kinetics of the reaction of oxygen with clean nickel single crystal surfaces : II. Ni(111) surface. *Surface Science.* **43**, 141 (1974).

3. S. Aggarwal, A.P. Monga, S.R. Perusse, R. Ramesh, V. Ballarotto, E.D. Williams, B.R. Chalamala, Y. Wei, and R.H. Reuss: Spontaneous ordering of oxide nanostructures. *Science.* **287**, 2235 (2000).

4. S. Aggarwal, S.B. Ogale, C.S. Ganpule, S.R. Shinde, V.A. Novikov, A.P. Monga, M.R. Burr, R. Ramesh, V. Ballarotto, and E.D. Williams: Oxide nanostructures through self-assembly. *Applied Physics Letters.* **78**, 1442 (2001).

5. S.R. Shinde, A.S. Ogale, S.B. Ogale, S. Aggarwal, V. Novikov, E.D. Williams, and R. Ramesh: Self-organized pattern formation in the oxidation of supported iron thin films. I. An experimental study. *Physical Review B.* **64**, 035408 (2001).

6. K. Thurmer, E. Williams, and J. Reutt-Robey: Autocatalytic oxidation of lead crystallite surfaces. *Science.* **297**, 2033 (2002).

7. G.W. Zhou, *DYNAMICS OF COPPER OXIDATION INVESTIGATED BY IN SITU UHV-TEM*, PhD thesis, *Department of Materials Science and Engineering*. 2003, University of Pittsburgh: Pittsburgh. p. 161.

8. N.P. Padture, M. Gell, and E.H. Jordan: Materials science - Thermal barrier coatings for gas-turbine engine apptications. *Science.* **296**, 280 (2002).

9. A.G. Evans, D.R. Mumm, J.W. Hutchinson, G.H. Meier, and F.S. Pettit: Mechanisms controlling the durability of thermal barrier coatings. *Progress in Materials Science.* **46**, 505 (2001).

10. *International Technology Roadmap for Semiconductors*. 2003: Semiconductor Industry Association.

11. H. Over, Y.D. Kim, A.P. Seitsonen, S. Wendt, E. Lundgren, M. Schmid, P. Varga, A. Morgante, and G. Ertl: Atomic-scale structure and catalytic reactivity of the RuO2(110) surface. *Science.* **287**, 1474 (2000).

12. B. Delmon, *Handbook of Heterogeneous Catalysis*, in *Handbook of Heterogeneous Catalysis*, G. Ertl, H. Knozinger and J. Weitkamp, Editors. 1997, Wiley-VCH: New York, U.S.A. p. 264.

13. D.J. Coulman, J. Wintterlin, R.J. Behm, and G. Ertl: Novel Mechanism for the Formation of Chemisorption Phases - the (2x1)O-Cu(110 Added-Row Reconstruction. *Physical Review Letters.* **64**, 1761 (1990).

14. L. Eierdal, F. Besenbacher, E. Laegsgaard, and I. Stensgaard: Interaction of Oxygen with Ni(110) Studied by Scanning-Tunneling-Microscopy. *Surface Science.* **312**, 31 (1994).

15. C.I. Carlisle, T. Fujimoto, W.S. Sim, and D.A. King: Atomic imaging of the transition between oxygen chemisorption and oxide film growth on Ag{111}. *Surface Science.* **470**, 15 (2000).

16. J.C. Yang, D. Evan, and L. Tropia: From nucleation to coalescence of Cu2O islands during in situ oxidation of Cu(001). *Applied Physics Letters.* **81**, 241 (2002).

17. G.W. Zhou, and J.C. Yang: Formation of quasi-one-dimensional Cu2O structures by in situ oxidation of Cu(100). *Physical Review Letters.* **89**, 106101 (2002).

18. J.C. Yang, M. Yeadon, B. Kolasa, and J.M. Gibson: Oxygen surface diffusion in three-dimensional Cu2O growth on Cu(001) thin films. *Applied Physics Letters.* **70**, 3522 (1997).

19. G.W. Zhou, and J.C. Yang: Temperature effect on the Cu2O oxide morphology created by oxidation of Cu(001) as investigated by in situ UHV TEM. *Applied Surface Science.* **210**, 165 (2003).

20. J. Tersoff: Oscillatory Segregation at a Metal Alloy Surface - Relation to Ordered Bulk Phases. *Physical Review B.* **42**, 10965 (1990).

21. M. Polak, and L. Rubinovich: The interplay of surface segregation and atomic order in alloys. *Surface Science Reports.* **38**, 129 (2000).

22. U. Bardi: The Atomic-Structure of Alloy Surfaces and Surface Alloys. *Reports on Progress in Physics.* **57**, 939 (1994).

23. I.K. Robinson, and P.J. Eng: Near-Surface and Bulk Short-Range Order in Cu3au. *Physical Review B.* **52**, 9955 (1995).

24. G.W. Graham: Oxygen-Adsorption on Cu3au(100) above 350-K. *Surface Science.* **137**, L79 (1984).

25. H. Niehus, and C. Achete: Surface-Structure Investigation of Nitrogen and Oxygen on Cu3Au(100). *Surface Science.* **289**, 19 (1993).

26. S. Nakanishi, K. Kawamoto, N. Fukuoka, and K. Umezawa: Low-Energy Ion-Scattering Analysis of the Surface Compositional Change of Au3cu(001) Induced by Oxygen-Chemisorption. *Surface Science.* **261**, 342 (1992).

27. M. Kastner, and B. Voigtlander: Kinetically self-limiting growth of Ge islands on Si(001). *Physical Review Letters.* **82**, 2745 (1999).

28. G.W. Zhou, and J.C. Yang: Initial oxidation kinetics of copper (110) film investigated by in situ UHV-TEM. *Surface Science.* **531**, 359 (2003).

29. G.W. Zhou, and J.C. Yang: Temperature effects on the growth of oxide islands on Cu(110). *Applied Surface Science.* **222**, 357 (2004).

30. J.C. Yang, Yeadon, M., Kolasa, B., Gibson, J.M.: *Scripta Materialia.* **38**, 1237 (1998).

31. M. Ohring, in *The Materials Science of Thin Films*. 2001, Academic Press: San Diego. p. 380.

32. J.A. Venables: *Phil. Mag.,.* **27**, 697 (1973).

33. J.W. Evans, and M.C. Bartelt: Island sizes and capture zone areas in submonolayer deposition: Scaling and factorization of the joint probability distribution. *Physical Review B.* **66**, (2002).

34. W.H. Orr, Ph.D thesis. 1962, Cornell University.

35. P.H. Holloway, Hudson, J.B.: *Surface Science.* **43**, 123 (1974).

36. Li Sun, Liang Wang, and J.C. Yang: The Low Temperature Initial Oxidation Stages of Cu (100) Investigated by In situ UHV-TEM. *Submitted to Journal of Materials Research.* (2004).

37. J. Tersoff, and R.M. Tromp: Shape Transition in Growth of Strained Islands - Spontaneous Formation of Quantum Wires. *Physical Review Letters.* **70**, 2782 (1993).

38. P.R. Markworth, Liu, X., Dai, J.Y., Fan, W., Marks, T.J., Chang, R.P.H.: *J. Mater. Res.* **16**, 2408 (2001).

39. K.R. Lawless, and Gwathmey, A.T.: *Acta Metall.* **4**, 153 (1956).

40. F. Young, Cathcart, J., and Gwathmey, A.: *Acta Metall.* **4**, 145 (1956).

41. A.T. Gwathmey, Lawless, K.R., *The Surface Chemistry of Metals and Semiconductors*, H.C. Gatos, Editor. 1960, John Wiley and Sons, Inc.: New York. p. 483.

42. J. Bardolle, Benard, J.: *Rev. Met.* **49**, 613 (1952).

43. J. Benard, Gronlund, F., Oudar, Jr., Duret, M.: *Z. Elektrochem. Ber. Bunsenges Physik, Chem.* **63**, 799 (1959).

44. K. Tanaka, Fujita, T., and Okawa, Y.: *Surface Science.* **401**, L407 (1998).

45. F.M. Leibsle: *Surface Science.* **337**, 51 (1998).

46. T. Lederer, Arvanitis, D., Comelli, G., Troger, L., Baberschke, K.: *Phys. Rev. B.* **48**, 15390 (1993).

47. P.J. Knight, Driver, S.M., Woodruff, D.P.: *J Phys-Condens Mat.* **9**, 21 (1997).

48. D.J. Coulman, Wintterlin, J., Behm, R.J., Ertl, G.: *Phys. Rev. Lett.* **64**, 1761 (1990).

49. W.W. Mullins: *Phil. Mag.* **6**, 1313 (1961).

50. B.M. Ocko, Mochrie, S.G.J.: *Phys. Rev. B.* **38**, 7378 (1988).

51. G.W. Zhou, L. Wang, and J.C. Yang: Effects of surface topology on the formation of oxide islands on Cu surfaces. *Accepted by Journal of Applied Physics.* (2005).

52. F. Jensen, Besenbacher, F., Lagsgaard, E., Stensgaard, I.: *Surface Science.* **259**, l781 (1991).

53. F. Jensen, Besenbacher, F., Stensgaard, I.: *Surface Science.* **269/270**, 400 (1992).

54. F. Besenbacher, and Norskov, J.K.: *Progress in Surface Science.* **44**, 5 (1993).

55. T. Matsumoto, Bennett, R.A., Stone, P., Yamada, T., Domen, K., Bowker, M.: *Surface Science.* **471**, 225 (2001).

56. L.E. Murr, and Inman, M.C.: *Phil. Mag.* 135 (1966).

57. R.B. Kehoe: *Phil. Mag.* 455 (1956).

58. G. Safran, Geszti, O., and Barna, P.B: *Phys. Stat. Sol. (A).* **150**, 489 (1995).

59. C. Zimmermann, in *Department of Physics*. 2000, University of Augsburgh: Germany.

60. M.L. Mcdonald, J.M. Gibson, and F.C. Unterwald: Design of an Ultrahigh-Vacuum Specimen Environment for High-Resolution Transmission Electron-Microscopy. *Review of Scientific Instruments.* **60**, 700 (1989).

61. M. Gao, J.M. Zuo, R.D. Twesten, I. Petrov, L.A. Nagahara, and R. Zhang: Structure determination of individual single-wall carbon nanotubes by nanoarea electron diffraction. *Applied Physics Letters.* **82**, 2703 (2003).

62. P.B. Hirsch, A. Howie, R.B. Nicholson, D.W. Pashley, and M.J. Whelan, Electron Microscopy of Thin Crystals. 2nd Ed. ed. 1977, Huntington, NY: Krieger. 19.

63. N.D. Browning, D.J. Wallis, P.D. Nellist, and S.J. Pennycook: EELS in the STEM: Determination of materials properties on the atomic scale. *Micron.* **28**, 333 (1997).

64. G.W. Zhou, and J.C. Yang: Unpublished result.

65. J.C. Yang, M. Yeadon, B. Kolasa, and J.M. Gibson: The homogeneous nucleation mechanism of Cu2O on Cu(001). *Scripta Materialia.* **38**, 1237 (1998).

66. R.W.G. Wychoff, Crystal Structures. 2nd Ed. ed. 1963: Wiley, New York.

67. M. Yeadon, J.C. Yang, R.S. Averback, J.W. Bullard, and J.M. Gibson: In-situ TEM study of the sintering of copper nanoparticles on (001) copper. *Electron Microscopy and Analysis 1997.* 257 (1997).

68. *Diffusion Data*. 1968. p. 116.

69. L.P.H. Jeurgens, W.G. Sloof, F.D. Tichelaar, and E.J. Mittemeijer: Thermodynamic stability of amorphous oxide films on metals: Application to aluminum oxide films on aluminum substrates. *Physical Review B.* **62**, 4707 (2000).

70. D.R. Gaskell, Introduction to metallurgical thermodynamics. escond edition ed. 1981, New York: McGraw-Hill book company.

71. P.R. Markworth, X. Liu, J.Y. Dai, W. Fan, T.J. Marks, and R.P.H. Chang: Coherent island formation of Cu2O films grown by chemical vapor deposition on MgO(110). *Journal of Materials Research.* **16**, 2408 (2001).

72. F. Family, and P. Meakin: Scaling of the Droplet-Size Distribution in Vapor-Deposited Thin-Films. *Physical Review Letters.* **61**, 428 (1988).

73. M. Zinke-Allmang, L.C. Feldman, and M.H. Grabow: Clustering on Surfaces. *Surface Science Reports.* **16**, 377 (1992).

74. B. Straumal, E. Rabkin, W. Gust, and B. Predel: The Influence of an Ordering Transition on the Interdiffusion in Au-Cu Alloys. *Acta Metallurgica Et Materialia.* **43**, 1817 (1995).

75. K.N. Tu, and B.S. Berry: X-ray study of interdiffusion in bimetallic Cu-Au films. *J. Appl. Phys.* **43**, 3283 (1972).

76. G.W. Zhou, L. Wang, R.C. Birtcher, P.M. Baldo, J.E. Pearson, J.C. Yang, and J.A. Eastman: Kinetics in the early-stage oxidation of (100)Cu-Au alloys investigated by in situ TEM. *Prepared for Appl. Phys. Lett.* (2005).